ISSN:1575-6807
D.L.: GC-1317-1999

INSTITUTO UNIVERSITARIO DE CIENCIAS Y TECNOLOGIAS CIBERNETICAS

Geometric Invariant Shape Representation using Morphological Multiscale Analyses and Applications to Shape Classification

L. Alvarez – A.P. Blanc – L.Mazorra – F.Santana

Nº 0020

April 2002

Cuadernos del Instituto Universitario de Ciencias y Tecnologías Cibernéticas
Instituto Universitario de Ciencias y Tecnologías Cibernéticas
Universidad de Las Palmas de Gran Canaria
Campus de Tafira
35017 Las Palmas, España
http://www.iuctc.ulpgc.es

Geometric Invariant Shape Representation using Morphological Multiscale Analyses and Applications to Shape Classification

L.Alvarez, A-P.Blanc, L.Mazorra and F.Santana

Departamento de Informática y Sistemas

Universidad de Las Palmas de Gran Canaria

Campus de Tafira, 35017 Las Palmas, Spain

WWW: http://serdis.dis.ulpgc.es/ami

April 2002

Abstract

This is a revised version of paper [2]. We have putted together papers [2] and [1], and we have included a lot of changes in order the paper be more understandable, readable and complete, we have also included a new application of the technique to the problem of shape classification. We present a new geometric invariant shape representation using morphological multiscale analyses. The geometric invariant is based on the area and perimeter evolution of the shape under the action of a morphological multiscale analysis. First, we present some theoretical results on the perimeter and area evolution across the scales of a shape. In the case of similarity transformations, the proposed geometric invariant is based on a scale-normalized evolution of the isoperimetric ratio of the shape. In the case of general affine geometric transformations the proposed geometric invariant is based on a scale-normalized evolution of the area. We present some numerical experiments to evaluate the performance of the proposed models. We present an application of this technique to the problem of shape classification on a real shape database and we study the well-posedness of the proposed models in the framework of viscosity solution theory.

1 Introduction.

Shape representation methods play an important role in systems for object recognition and analysis. According to the classification of shape analysis methods proposed by [26] and [21], by shape representation methods we mean methods which provide a non-numeric representation of the shape (e.g. a graph). Shape description refers to the methods that result in a numeric descriptor of the shape and could be a step subsequent to shape representation. Another classification of shape analysis methods is based on the use of shape boundary points as opposed to the interior of the shape. The two resulting classes of methods are known as boundary (also called external) and global (also called internal), respectively.

In the last years, multiscale analyses have became a common tool for many tasks in computer vision. A multiscale analysis can be defined as an operator $T_t(f)$ which provides for an original image f a sequence of images $T_t(f)$ which represent the image at a coarse scale t.

In this paper we deal with morphological multiscale analyses, which satisfy the morphological invariance, that is, the multiscale analysis $T_t(f)$ commutes with any increasing histogram modification of the image. It means that for any increasing function $g(.)$

$$T_t(f) \circ g = T_t(f \circ g).$$

The underlying hypothesis associated to this morphological invariance is that the contrast between the different objects present in the image is not important at all, and that all the information present in the image is described by the geometry of the level sets of the image. In particular, the way a shape changes under the action of a morphological multiscale analysis depends only on the geometry of its boundary.

The main goal of this paper is to use the nice geometric and morphological invariant properties of the morphological multiscale analyses in order to find out a reliable global shape representation. Linear scale-space shape representations have been studied by different authors in the literature: [30] proposed a scale space filtering approach by tracking the position of the inflection points in signals filtered by gaussians. [8] proposed a representation called *the curvature primal sketch.* The shape boundary is filtered with gaussian functions of increasing width to obtain a boundary curvature-based multiscale representation of the shape. [25] also propose a scale-space boundary shape representation based on the curvature evolution across the scales. In the context of the morphological scale spaces, [22] proposed the pattern spectrum representation based on the area evolution of a shape obtained by opening the shape with a disk of increasing size. [11] and [12], proposed a method for affine invariant shape recognition based on the affine invariant morphological multiscale analysis. They use the multiscale analysis to recover characteristic points in the shape. [13], use the affine invariant multiscale analysis to smooth the images before a local encoding of the shape elements.[20] introduced the named reaction-diffusion space where they combine constant and curvature deformation for shape analysis.

The main underlying idea we propose in this paper is that if we take any global invariant of a shape and we follow the evolution of such invariant under the action of a morphological multiscale analysis then, this evolution is also un invariant of the shape, but it contains much more robust and discriminant information of the geometry of the shape that just the invariant for the initial shape. In particular, we propose in this paper to use the evolution of the area and/or perimeter of the shape across the scales under the action of different morphological multiscale analyses as basic tools to find out scale-space global shape representation. The main advantage of the morphological multiscale analyses with respect to the classical linear-scale space is that the evolution of the shape depends just on the geometry of the shape and it is not depends at all on the contrast of the shape with respect to the background or the relative location of other shapes presented in the image which is not the case in the linear scale-space where the way a shape evolves depends on the contrast and location with respect to other shapes presented in the image.

As it was proved by [3], under some minimal architectural assumptions, all the morphological and similarity invariant multiscale analyses are generated by the partial differential equation:

$$\frac{\partial u}{\partial t} = \beta(t\, curv(u)) \left\| \nabla u \right\|, \tag{1}$$

where $\beta(.)$ is a nondecreasing function and $curv(u)(x, y)$ is the curvature of the level line passing by the point (x, y), that is:

$$curv(u) = div \left(\frac{\nabla u}{\|\nabla u\|} \right). \tag{2}$$

Therefore if $u(t, x, y)$ is the solution of equation (1), for the initial datum f, then

$$u(t, x, y) = T_t(f)(x, y).$$

In order to simplify a bit the model, we are going to remove the t dependence inside the term $\beta(t\, curv(u))$, that is we consider the equation:

$$\frac{\partial u}{\partial t} = \beta(curv(u)) \left\| \nabla u \right\|. \tag{3}$$

We can show easily that with this change in the equation, the underlying multiscale analysis keep the morphological and Euclidean transformation invariant, but it loss, in general, the zoom invariant. We are going to show that in order to recover the zoom invariant we have to fit the function $\beta(s)$ to be a polynomial. We notice that these morphological multiscale analyses are also invariant under symmetry transformations $((x, y) \to (\pm x, \pm y))$.

Following the morphological principle, we will consider that a shape S_0 is given by a level set of the image f, that is:

$$S_0 = \overline{\{(x, y) :\ f(x, y) < \lambda\}},$$

for some λ, where for a set A, we denote by $\overline{A}$ the closure of A, that is, the minimum closed set including A. We will denote by $S(t)$ the evolution across the scales of S_0, that is:

$$S(t) = \overline{\{(x, y) :\ T_t(f)(x, y) < \lambda\}}.$$

We will also denote by $C(t)$ the boundary of $S(t)$. For the case $C(t)$ is a family of single Jordan curves, we can interpret the evolution of $C(t)$ in terms of curve evolution. In fact, $C(t)$ is a solution to the curve evolution equation

$$\frac{\partial C}{\partial t} = \beta(k)\vec{N}, \tag{4}$$

where $\vec{N}$ represents the unit inward normal direction to the curve $C(t)$ and k is the curvature. In the last years, a lot research have been devoted to this curve evolution equation see, for instance, [4], [5], [6],[14], [15], [16], [3], [7], [27].

The organization of the paper is as follows: In section 2, we present some theoretical results on the area and perimeter evolution of a shape under the action of a morphological multiscale analysis. In section 3, we analyze the similarity invariant shape representation, and we propose as geometric invariant a scale-normalized isoperimetric ratio evolution. In section 4, we study the affine invariant shape representation, and we propose as geometric invariant a scale-normalized area ratio evolution. In section 5, we present some numerical experiments. In section 6 we present an application of the proposed models to the classification of shapes in a real sea animals shape database. In section 7 we present some conclusions. Finally, in an appendix we show the mathematical justification of some of the results we present in this paper, and we study the well-posedness of the models we propose in the framework of the viscosity solution theory.

2 Area and perimeter evolution of a shape under the action of a morphological multiscale analysis

First, we notice that the function $|S(t)| = Area(S(t))$ and $|C(t)| = Perimeter(C(t)$ are Euclidean invariants of S_0. Indeed, since the multiscale analysis (3) is invariant under Euclidean transformations, given two shapes S_0, S_0', $S(t)$, $S'(t)$ its corresponding evolutions, such that there exists a Euclidean transformation E satisfying $S_0' = E(S_0)$, then

$$|S(t)| = |S'(t)| \quad for\ any\ t > 0$$
$$|C(t)| = |C'(t)| \quad for\ any\ t > 0.$$

Therefore the function $t \to |S(t)|$ and $t \to |C(t)|$ are Euclidean invariants of the shape S_0.

In this section, we will show formulas for the evolution of perimeter and area, of a shape, following equation (3). The results that we present here are a generalization of the ones presented in [16] for the Euclidean shortening flow which corresponds to the particular choice $\beta(s) = s$. We will assume that for some $t_0 > 0$, $C(t)$, the boundary of the shape $S(t)$ at scale t, is a family of single Jordan curves for $0 \leq t < t_0$. We notice that since a Jordan curve can not be empty, then the perimeter and area of the shape is always properly defined.

Proposition 1 *If for $0 \leq t < t_0$, $C(t)$ is a family of single Jordan curves, then the evolution across the scales of the length of the curve $|C(t)|$ under the action of (3), is given by*

$$\frac{\partial |C(t)|}{\partial t} = -\int_0^{|C(t)|} k\beta(k)ds, \tag{5}$$

with s the arclength along the curve and k the curvature.

Proof : see appendix.
Remark : As a special case, when $\beta(k)$ is a constant $(\beta(k) \equiv M)$, we have:

$$\frac{\partial |C(t)|}{\partial t} = -M \int_0^{|C(t)|} kds = -2\pi M,$$

and therefore:

$$|C(t)| = |C(0)| - 2\pi Mt.$$

So in this particular case, the evolution of the perimeter $|C(t)|$ does not depend on the geometry of $C(t)$, and therefore, $|C(t)|$ can not be used to discriminate between different shapes.

Proposition 2 *If for $0 \leq t < t_0$, $C(t)$ is a family of single Jordan curves, then the evolution across the scales of the area $|S(t)|$ under the action of (3), is given by*

$$\frac{\partial |S(t)|}{\partial t} = -\int_0^{|C(t)|} \beta(k)ds. \tag{6}$$

Proof : See appendix.
Remark : when $\beta(k) = k$, which corresponds to the mean curvature motion equation, we have:

$$\frac{\partial |S(t)|}{\partial t} = -\int_0^{|C(t)|} k ds = -2\pi,$$

and therefore:

$$|S(t)| = |S_0| - 2\pi t.$$

So in this case, the evolution of the area $|S(t)|$ does not depend on the geometry of $C(t)$, and therefore $|S(t)|$ can not be used to discriminate between different shapes. We notice that this result is true only for the particular choice $\beta(s) = s$, and that in general, for other values of $\beta(s)$ the evolution of the area depends on the geometry of S_0.

Remark. The results presented above concerns the case of shapes without holes, that is, the contour is just a single Jordan curve. However, we can easily extend the results to shapes with a finite number of holes. That is, for instance, if for $0 \leq t < t_0$ the boundary of the shape under the action of the morphological multiscale analysis is given by a set of collections of Jordan curve evolution $C_i(t) \;\; for \;\; i = 0, .., N$ where C_0 is the exterior contour, then the area evolution of the shape is given by :

$$\frac{\partial |S(t)|}{\partial t} = -\int_0^{|C_0(t)|} \beta(k) ds + \sum_{i=1}^{N} \int_0^{|C_i(t)|} \beta(k) ds. \tag{7}$$

One interesting observation is that in the case $\beta(k) = k$ the area evolution of the shape would be given by

$$|S(t)| = |S_0| - 2(1 - N)\pi t,$$

where N represents the number of holes of the shapes. So in particular, we can detect the number of holes of a shape following the slope of the area evolution of the shape under the action of the mean curvature motion equation.

3 Morphological Similarity Invariant Representation of a Shape.

In this section, we are going to study how to find out a similarity invariant using the area and perimeter evolution of $S(t)$. A similarity transformation H is generated by rotations, translations and zooming, and it can be expressed in the following way:

$$H(x, y) = s \begin{pmatrix} \cos(\alpha) & \sin(\alpha) \\ -\sin(\alpha) & \cos(\alpha) \end{pmatrix} \begin{pmatrix} x \\ y \end{pmatrix} + \begin{pmatrix} a \\ b \end{pmatrix}$$

where α is the rotation angle, (a, b) the translation vector and s the zoom factor. We will say that a multiscale analysis is invariant under similarity transformations if for any similarity transformation H, there exists a function $t \to t'(H, t)$ such that

$$H\left(T_{t'(H,t)}(f)\right) = T_t(H(f)).$$

First, we will characterize the morphological multiscale analyses invariant under similarity transformation.

Proposition 3 *Let be $T_t(f)$ a morphological multiscale analysis given by (3). $T_t(f)$ is invariant under similarity transformations if and only if there exists a constant $p \geq 0$ such that:*

$$\beta(s) = \begin{cases} \beta(1)s^p & if \quad s \geq 0 \\ \beta(-1)\,(-s)^p & if \quad s < 0. \end{cases} \tag{8}$$

Moreover if s is the zoom factor of the similarity transformation H, then

$$t'(H,t) = s^{p+1}t.$$

Proof: See appendix.

Remark: We notice from the previous proposition that the multiscale analysis $T_t(f)$ is not scale invariant in the sense that a similarity transformation does not modify the space and scale variables in the same way, it means that if we apply a zoom $(x,y) \rightarrow (sx,sy)$ to the shape, then the scale is modified by $t \rightarrow s^{p+1}t \neq st$. In order to have the scale invariant property we need just to replace t with the new scale $\tilde{t}$ using the transformation:

$$\tilde{t} = (t(p+1))^{\frac{1}{p+1}}. \tag{9}$$

We then have that $(x,y,\tilde{t}) \rightarrow (sx,sy,s\tilde{t})$ under the action of the zoom transformation $H(x,y) = (sx,sy)$. Indeed,

$$H(T_{\tilde{t}s}(f)) = H(T_{\frac{(ts)^{p+1}}{p+1}}(f)) = T_{\frac{(t)^{p+1}}{p+1}}(H(f)) = T_{\tilde{t}}(H(f)).$$

The new scale variable $\tilde{t}$ has a more physical meaning. For instance a circle of radius R_0 vanishes in a scale proportional to $\tilde{t} = R_0$ (see lemma 3 in the appendix for more details). In the particular case of $\beta(1) = 1$, the vanishing scale of a circle (that is, the scale at the circle disappears) is equal to its radius, so we can interpret that at the scale $\tilde{t}$, all the objects initially included in a disk of radius $\tilde{t}$ have been removed by the multiscale analysis. So, in some way, the scale variable $\tilde{t}$ represents the resolution of the morphological multiscale analysis.

Remark: We notice that, in fact, the similarity invariant morphological multiscale analysis depends on 3 parameters, the power $p \geq 0$ and the constant $\beta_{-1} = \beta(-1)$ and $\beta_1 = \beta(1)$ which are not completely free because the function $\beta(s)$ has to be nondecreasing. It means that if $p > 0$ then $\beta_1 \geq 0$ and $\beta_{-1} \leq 0$. In what follows we will represent the similarity invariant multiscale analyses $T_t(f)$ by these 3 parameters, that is :

$$T_t(f) = T_t^{(p,\beta_{-1},\beta_1)}(f).$$

We will use also the notation

$$\begin{array}{l} S_{(p,\beta_{-1},\beta_1)}(t) \\ C_{(p,\beta_{-1},\beta_1)}(t), \end{array}$$

to indicate the evolution of the shape S_0 and its boundary C_0 following the multiscale analysis given by parameters (p,β_{-1},β_1).

We notice that if we add to the morphological multiscale analysis the invariance under the inversion of the histogram (that is to change f by $-f$) then we can deduce easily (for $p > 0$)

that β_1 have to be equal to $-\beta_{-1}$. In what follow we are not going to assume this invariance in order to have the possibility to choose different relations between the parameters β_1 and β_{-1}. Anyway we will see in section 6 that by combining several morphological multiscale analyses we can get distance criteria between shapes which are invariant under histogram inversion transformations.

Among the different possibilities of similarity invariant morphological multiscale analyses let us mention 3 examples which correspond to some particular choices for (p, β_{-1}, β_1). The first example is given for the classical mathematical morphology operators dilation and erosion, which corresponds to the choices

$$(p, \beta_{-1}, \beta_1) = (0, 1, 1) \tag{10}$$
$$(p, \beta_{-1}, \beta_1) = (0, -1, -1). \tag{11}$$

See for instance [3] for more details about the relation between the classical mathematical morphology operators and the choice of (p, β_{-1}, β_1) presented above. The second example of multiscale analysis is based on the mean curvature motion operator, where we have typically 3 options for the choices of (p, β_{-1}, β_1):

$$\begin{aligned} (p, \beta_{-1}, \beta_1) &= (1, -1, 1) \\ (p, \beta_{-1}, \beta_1) &= (1, 0, 1) \\ (p, \beta_{-1}, \beta_1) &= (1, -1, 0). \end{aligned} \tag{12}$$

The third example of multiscale analysis that we consider is based on the affine invariant multiscale analysis discovered by [3] and [27] in an independent way. In this case, we will use, again, 3 different choices for (p, β_{-1}, β_1):

$$\begin{aligned} (p, \beta_{-1}, \beta_1) &= (\frac{1}{3}, -1, 1) \\ (p, \beta_{-1}, \beta_1) &= (\frac{1}{3}, 0, 1) \\ (p, \beta_{-1}, \beta_1) &= (\frac{1}{3}, -1, 0). \end{aligned} \tag{13}$$

In figure 1 we illustrate a shape contour evolution under the action of a morphological multiscale analysis. In the exterior contour of the shape, the evolution of the convexe part of the contour is governed by parameter β_1, and the evolution of the concave part of the contour is governed by parameter β_{-1}. In the contour of the hole of the shape is the opposite, that is the convexe part is governed by β_{-1}, and the concave part by β_1 (the reason is that in the contour of the holes the sign of the curvature, using equation (2), changes). Therefore if we take $p > 0$ and $(\beta_{-1}, \beta_1) = (-1, 1)$, what we expect is that both contours (exterior and interior), under the action of the multiscale analysis, tend to disappear in an independent way, and the concave parts tend to change to convexe. However if we take $(\beta_{-1}, \beta_1) = (0, 1)$, then the concave part of the exterior contour remains fix (as far as they remain concave), and the convexe part of the hole remains fix. So for the shape of figure 1 we expect that the convexe part of the exterior contours evolves, the interior disk remains fix, so a singularity is going to be developed when the exterior contour touches the interior disk. So, we note that the evolution is completely different with respect to the case $(\beta_{-1}, \beta_1) = (-1, 1)$, and it provides a completely different information about the geometry of the shape. In a similar way, if we take $(\beta_{-1}, \beta_1) = (-1, 0)$, then, we expect that the convexe part of the exterior contour remains fix and the concave part of the exterior contour and the inside hole moves, so what happens, as it is shown in the appendix, is that asymptotically the shape converges towards the convexe hull of the initial shape. So we note that combining the information of the evolutions for the 3 cases $(\beta_{-1}, \beta_1) \in \{(-1, 1), (0, 1), (-1, 0)\}$ we obtain a fruitful information about the shape geometry, and it is exactly what we will use later to get a discriminant shape representation. Of course we can choose any other set of values for the parameter (p, β_{-1}, β_1) but we think that the choice we make above are, in some way representative, first, because, the values $p = 1, \frac{1}{3}$, correspond to the classic exponent for curvature evolution in the Euclidean and affine case and combining the values of $(\beta_{-1}, \beta_1) \in \{(-1, 1), (0, 1), (-1, 0)\}$ we characterize in a powerful way the shape following the geometry of their concave and convexe part.

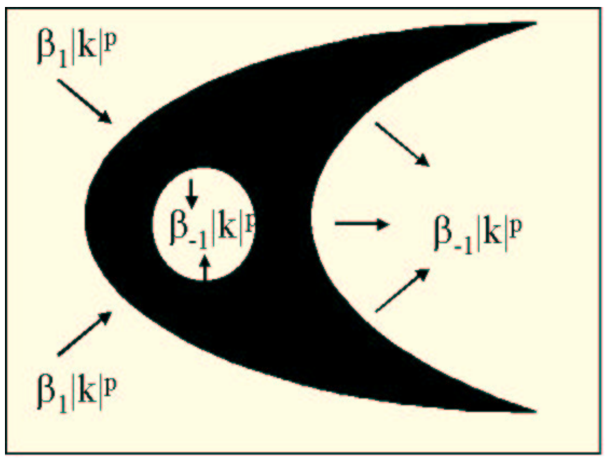

Figure 1: Illustration of a shape contour evolution under the action of a morphological multiscale analysis

Remark. Another interesting morphological multiscale analysis used for shape analysis is the named reaction-diffusion space introduced in [20]. This multiscale analysis is generated by the curve evolution equation:

$$\frac{\partial C}{\partial t} = (\beta_0 + \beta_1 k)\vec{N}, \tag{14}$$

where β_0, β_1 are 2 parameters. An interesting remark is that this multiscale analysis is morphological and Euclidian invariant but it is not similarity invariant (it is not zoom invariant) However we can transform very easily the equation in order to get the zoom invariant, indeed, if we take the equation

$$\frac{\partial C}{\partial t} = (\beta_0 + \beta_1 k\, t)\vec{N}, \tag{15}$$

then, following the general result showed in [3], we get a similarity invariant multiscale analysis. With this change it could be very interesting to reproduce the analysis we make here using this "new" reaction-diffusion scale-space, but this is beyond the scope of this paper.

The scale-normalized isoperimetric ratio evolution.

In order to find out similarity invariants we have to normalize the scale following the zoom factor s. First we notice that if $T_t^{(p,\beta_{-1},\beta_1)}(f)$ is a morphological multiscale analysis invariant under similarity transformations, S_0, S_0' bounded shapes, and H a similarity transformation such that $H(S_0')=S_0$, then using proposition 3, and (9) we obtain

$$\begin{aligned} S_{(p,\beta_{-1},\beta_1)}(\tilde{t}) &= H(S'_{(p,\beta_{-1},\beta_1)}(s\tilde{t})) \quad for\ any\ t\geq 0 \\ \left|S_{(p,\beta_{-1},\beta_1)}(\tilde{t})\right| &= \frac{\left|S'_{(p,\beta_{-1},\beta_1)}(s\tilde{t})\right|}{s^2} \quad for\ any\ t\geq 0 \quad and \\ \left|C_{(p,\beta_{-1},\beta_1)}(\tilde{t})\right| &= \frac{\left|C'_{(p,\beta_{-1},\beta_1)}(s\tilde{t})\right|}{s} \quad for\ any\ t\geq 0. \end{aligned} \tag{16}$$

We will use as similarity invariant of a bounded shape S_0 the scale-normalized isoperimetric ratio evolution $I^{S_0}_{(p,\beta_{-1},\beta_1)}(\tilde{t})$ given by the following definition

Definition 1 *Let S_0 be a bounded shape. We define the scale-normalized isoperimetric ratio evolution $I^{S_0}_{(p,\beta_{-1},\beta_1)}(\tilde{t})$ as the function*

$$I^{S_0}_{(p,\beta_{-1},\beta_1)}(\tilde{t}) = 4\pi\frac{\left|S_{(p,\beta_{-1},\beta_1)}(\tilde{t}\sqrt{|S_0|})\right|}{\left|C_{(p,\beta_{-1},\beta_1)}(\tilde{t}\sqrt{|S_0|})\right|^2}.$$

We notice that $I^{S_0}_{(p,\beta_{-1},\beta_1)}(\tilde{t})\leq 1$, and $I^{S_0}_{(p,\beta_{-1},\beta_1)}(\tilde{t})=1$ only for the case when $S_{(p,\beta_{-1},\beta_1)}(\tilde{t}\sqrt{|S_0|})$ is a circle. Next, we will show that $I^{S_0}_{(p,\beta_{-1},\beta_1)}(\tilde{t})$ is a similarity invariant of the shape S_0.

Theorem 1 *Let $T_t^{(p,\beta_{-1},\beta_1)}(f)$ be a morphological multiscale analysis invariant under similarity transformations, S_0, S_0' be two bounded shapes such that there exists a similarity transformation H with $H(S_0')=S_0$, Then:*

$$I^{S_0}_{(p,\beta_{-1},\beta_1)}(\tilde{t}) = I^{S_0'}_{(p,\beta_{-1},\beta_1)}(\tilde{t}) \quad for\ \tilde{t}\geq 0.$$

Proof: Let s be the zoom factor of the transformation H, using (16) we obtain:

$$\begin{aligned} I^{S_0}_{(p,\beta_{-1},\beta_1)}(\tilde{t}) &= 4\pi\frac{\left|S_{(p,\beta_{-1},\beta_1)}(\tilde{t}\sqrt{|S_0|})\right|}{\left|C_{(p,\beta_{-1},\beta_1)}(\tilde{t}\sqrt{|S_0|})\right|^2} = 4\pi\frac{\left|S'_{(p,\beta_{-1},\beta_1)}(\tilde{t}s\sqrt{|S_0|})\right|}{\left|C'_{(p,\beta_{-1},\beta_1)}(\tilde{t}s\sqrt{|S_0|})\right|^2} = \\ &= 4\pi\frac{\left|S'_{(p,\beta_{-1},\beta_1)}(\tilde{t}\sqrt{|S_0'|})\right|}{\left|C'_{(p,\beta_{-1},\beta_1)}(\tilde{t}\sqrt{|S_0'|})\right|^2} = I^{S_0}_{(p,\beta_{-1},\beta_1)}(\tilde{t}). \end{aligned}$$

This concludes the proof.

Remark: We notice that in the case of the mean curvature evolution ($(p,\beta_{-1},\beta_1)=(1,-1,1)$), if $C(t)$ is a family of single Jordan curves, then, following the results of the previous section we have that

$$\left|S_{(1,-1,1)}(\tilde{t}\sqrt{|S_0|})\right| = |S_0|\left(1-\pi\tilde{t}^2\right)_+ \tag{17}$$

where $(1-\pi\tilde{t}^2)_+ = max(1-\pi\tilde{t}^2, 0)$. This gives a close form expression for the evolution of the area. Moreover, [15] show that $S_{(1,-1,1)}(t)$ converges towards a circle before vanishing and then, $I^{S_0}_{(1,-1,1)}(\tilde{t})$ satisfies:

$$\underset{\tilde{t}\to\left(\sqrt{\frac{1}{\pi}}\right)^-}{Lim} I^{S_0}_{(1,-1,1)}(\tilde{t}) = 1.$$

On the other hand, in the case $p=0$ we have that

$$\left|C_{(p,\beta_{-1},\beta_1)}(\tilde{t}\sqrt{|S_0|})\right| = \left(|C_0| - 2\pi\beta_1\tilde{t}\sqrt{|S_0|}\right)_+$$

this gives a close form expression for the evolution of the perimeter.

One interesting mathematical question is whether the isoperimetric ratio evolution is a monotone function or not. The experimental results suggest that it is true in the case of shapes defined by a single Jordan curve (that is without holes). However it seems quite difficult to show it except in the case $\beta_1 = 0$ where the result follows from relations (6) and (5). Indeed, in this case, from (6) and (5) we can deduce that the perimeter is a non-increasing function and the area is a non-decreasing function, then the isoperimetric ratio is a non-decreasing function.

4 Morphological Affine Invariant Representation of a Shape.

We consider a general affine transformation given by

$$H(x,y) = A\begin{pmatrix} x \\ y \end{pmatrix} + \begin{pmatrix} a \\ b \end{pmatrix}$$

where A is a 2×2 matrix with $|A| \neq 0$.

[3] show that the only affine invariant morphological multiscale analysis is given by

$$\beta(s) = \begin{cases} \beta_1 s^{\frac{1}{3}} & if \quad s \geq 0 \\ \beta_{-1}(-s)^{\frac{1}{3}} & if \quad s < 0, \end{cases}$$

where $\beta_1 \geq 0$ and $\beta_{-1} \leq 0$. In this case we have that

$$H\left(T_{t'(H,t)}(f)\right) = T_t(H(f)),$$

where

$$t'(H,t) = |A|^{\frac{4}{3}}\, t.$$

On the other hand, given two bounded shapes S_0, S'_0, such that there exists an affine transformation H with $H(S'_0) = S_0$, we have that:

$$\left|S_{(p,\beta_{-1},\beta_1)}(\tilde{t})\right| = \frac{\left|S'_{(p,\beta_{-1},\beta_1)}(\sqrt{|A|}\tilde{t})\right|}{|A|} \quad for\ any\ t \geq 0. \tag{18}$$

One of the main advantages of our approach is that we use a two parameters family of affine invariant scale spaces. In our knowledge we are the first to enjoy of such possibility, usually people take directly the classical case which correspond to $\beta_1 = -\beta_{-1}$. With this two parameters family, we can get much more information about the shape geometry that just using the classical affine invariant multiscale analysis.

In the case of the affine invariant representation, we can not use the scale-normalized isoperimetric ratio because the perimeter is not invariant under affine transformations. We propose a geometric invariant based just on the area evolution. However we note that we could use any other global affine invariant of the shape.

Next, We will introduce the scale-normalized area ratio.

Definition 2 *For a bounded shape S_0, we define the scale-normalized area ratio evolution $AR^{S_0}_{(p,\beta_{-1},\beta_1)}(\tilde{t})$ as the function*

$$AR^{S_0}_{(p,\beta_{-1},\beta_1)}(\tilde{t}) = \frac{\left|S_{(p,\beta_{-1},\beta_1)}(\tilde{t}\sqrt{|S_0|})\right|}{|S_0|}.$$

Next, we will show that $AR^{S_0}_{(p,\beta_{-1},\beta_1)}(\tilde{t})$ is an affine invariant of the shape S_0.

Theorem 2 *Let $T_t^{(\frac{1}{3},\beta_{-1},\beta_1)}(f)$ be a morphological multiscale analysis invariant under affine transformations ($p = \frac{1}{3}$), S_0, S_0' be two bounded shapes such that there exists an affine transformation H with $H(S_0') = S_0$, Then:*

$$AR^{S_0}_{(\frac{1}{3},\beta_{-1},\beta_1)}(\tilde{t}) = AR^{S_0'}_{(\frac{1}{3},\beta_{-1},\beta_1)}(\tilde{t}) \quad for\ \tilde{t} \geq 0.$$

Proof: Using (18) we obtain:

$$\begin{aligned} AR^{S_0}_{(\frac{1}{3},\beta_{-1},\beta_1)}(\tilde{t}) &= \frac{\left|S_{(\frac{1}{3},\beta_{-1},\beta_1)}(\tilde{t}\sqrt{|S_0|})\right|}{|S_0|} = \frac{\left|S'_{(\frac{1}{3},\beta_{-1},\beta_1)}(\tilde{t}\sqrt{|S_0|\,|A|})\right|}{|S_0|\,|A|} \\ &= \frac{\left|S'_{(\frac{1}{3},\beta_{-1},\beta_1)}(\tilde{t}\sqrt{|S_0'|})\right|}{|S_0'|} = AR^{S_0'}_{(\frac{1}{3},\beta_{-1},\beta_1)}(\tilde{t}), \end{aligned}$$

this concludes the proof.

Scale normalization using the vanishing scale.

Definition 3 *Given a morphological multiscale analysis $T_t^{(p,\beta_{-1},\beta_1)}(f)$ with $p \geq 0$ and a shape S_0, we define the vanishing scale $\tilde{t}_\infty^{(p,\beta_{-1},\beta_1)}(S_0)$ as the number:*

$$\tilde{t}_\infty^{(p,\beta_{-1},\beta_1)}(S_0) = \sup_{\tilde{t}>0}\{\left|S(\tilde{t})\right| > 0\}.$$

Remark: Let us note by $B_R(x,y)$ the circle of radius R centered in (x,y). The evolution of a circle under the action of a morphological multiscale analysis can be computed explicitly and it is given by the expression

$$S(\tilde{t}) = B_{\left(R^{p+1}-\beta_1\tilde{t}^{p+1}\right)_+^{\frac{1}{p+1}}}(x,y)$$

(see lemma 3 in the appendix for more details), therefore if $\beta_1 > 0$ the vanishing scale for a circle of radius R is given by:

$$\tilde{t}_\infty^{(p,\beta_{-1},\beta_1)}(B_R(x,y)) = \beta_1^{\frac{1}{p+1}} R.$$

On the other hand, if $\beta_1 > 0$ and S_0' is a bounded shape, then there exists a circle $B_{R_0}(x_0, y_0)$ such that $S_0' \subset B_{R_0}(x_0, y_0)$, and by the inclusion principle, which means that if a shape is included in another one, this relation is preserved by the multiscale analysis (see [4] for more details), we have:

$$S'(\tilde{t}) \subset B_{\left(R_0^{p+1} - \beta_1 \tilde{t}^{p+1}\right)_+^{\frac{1}{p+1}}}(x_0, y_0)$$

and therefore $\tilde{t}_\infty^{(p,\beta_{-1},\beta_1)}(S_0') < \beta_1^{\frac{1}{p+1}} R_0$.

Remark: We point out that under the action of a similarity or affine transformation, we have that $\tilde{t}_\infty^{(p,\beta_{-1},\beta_1)} \to s\tilde{t}_\infty^{(p,\beta_{-1},\beta_1)}$,where s is the zoom factor of the similarity transformation or $\tilde{t}_\infty^{(p,\beta_{-1},\beta_1)} \to \sqrt{|A|}\tilde{t}_\infty^{(p,\beta_{-1},\beta_1)}$ in the case of an affine transformation. This relation provides us another way to normalize the scale in the scale-normalized isoperimetric ratio and the scale-normalized area ratio. In other words the following functions are similarity (respect. affine) invariant of a shape

$$I_{(p,\beta_{-1},\beta_1)}^{S_0}(\tilde{t}) = \frac{\left|S_{(p,\beta_{-1},\beta_1)}\left(\tilde{t}(\tilde{t}_\infty^{(p,\beta_{-1}^*,\beta_1^*)})\right)\right|}{\left|C_{(p,\beta_{-1},\beta_1)}\left(\tilde{t}(\tilde{t}_\infty^{(p,\beta_{-1}^*,\beta_1^*)})\right)\right|^2}$$

$$AR_{(\frac{1}{3},\beta_{-1},\beta_1)}^{S_0}(\tilde{t}) = \frac{\left|S_{(\frac{1}{3},\beta_{-1},\beta_1)}\left(\tilde{t}(\tilde{t}_\infty^{(\frac{1}{3},\beta_{-1}^*,\beta_1^*)})\right)\right|}{\left(\tilde{t}_\infty^{(\frac{1}{3},\beta_{-1}^*,\beta_1^*)}\right)^2}.$$

So we can compute $\tilde{t}_\infty^{(p,\beta_{-1}^*,\beta_1^*)}$ for a particular choice of $(\beta_1^*, \beta_{-1}^*)$ and then we can normalize the scale with $\tilde{t}_\infty^{(p,\beta_{-1}^*,\beta_1^*)}$ for any other multiscale analysis (β_1, β_{-1}). For instance, we can estimate the vanishing scale for $(\beta_{-1}, \beta_1) = (-1, 1)$, and then, we can use this value to normalize the scale for $(\beta_{-1}, \beta_1) \in \{(-1,1), (0,1), (1,0)\}$

5 Numerical experiments

The numerical algorithms that we use to implement numerically the morphological multiscale analysis are based on the techniques studied in [4]. We use a simple explicit finite difference scheme to discretize equation (3). We have focussed our attention on the qualitative behavior of the proposed models and we have not devoted a lot of time to study the efficiency of the numerical algorithms. Of course, we could use more efficient algorithms to estimate the shape evolution like the ones studied in [28] or in [9] where they propose very fast and accurate curve evolution algorithms for equation (3). However the application of these curve evolution type algorithms could be delicate in some cases due to, on the one hand, the boundary of a shape could be defined by several curves (in the case the shape has holes) and on the other hand, as we are going to see, the evolution of the shape under the action of a morphological multiscale analysis can develop singularities in the shape evolution, that is the shape can

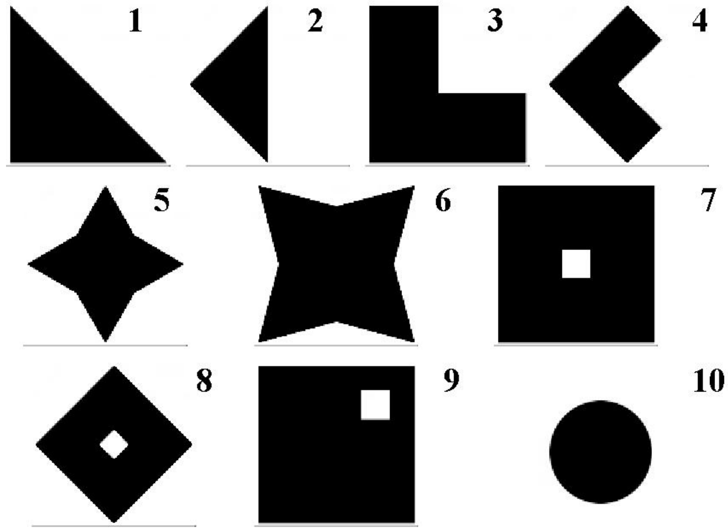

Figure 2: Test shapes used to evaluate the scale-normalized isoperimetric ratio.

be split in several shapes, two boundary curves can touch each other and become a single curve, etc...

Next, we will present some experiments using the scale normalized isoperimetric ratio evolution $I^{S_0}_{(1,\beta_{-1},\beta_1)}(\tilde{t})$. We will use some synthetic shapes given in figure 2. All the shapes (except the circle) have similar initial isoperimetric ratio (in fact theoretically the isoperimetric ratio is exactly the same for all shapes. However, in practice, because of pixel noise and numerical errors, the computed isoperimetric ratio is not the same), therefore the isoperimetric ratio for the initial shapes, is not useful at all to classify this synthetic shape database. However, as we are going to see, when we follow the evolution of the isoperimetric ratio under the action of a morphological multiscale analysis we can discriminate easily between the different shapes. The shapes are organized as follow: For each shape we have evaluated a similarity transformation where we have rotated and changed the size of the original shape. So shapes $1-2$, $3-4$, $4-5$, $5-6$ and $7-8$ are equivalent modulus a similarity transformation. Shape 9 is similar to shape 7 but in shape 9, we have changed the location of the inside square. We will compare $I^{S_0}_{(1,\beta_{-1},\beta_1)}(\tilde{t})$ for the different shapes for $\tilde{t} \in [0, 0.3]$. We recall that

$$\underset{\tilde{t}\to\left(\sqrt{\frac{1}{\pi}}\right)^-}{Lim} I^{S_0}_{(1,-1,1)}(\tilde{t}) = 1.$$

Therefore $\tilde{t} = \sqrt{\frac{1}{\pi}} \simeq 0.56$ is the upper bound for the scale comparison. In practice, we are not interested in taking this upper bound as final scale because the isoperimetric ratio is going to be close to 1 for any shape when we approach the upper bound scale and it is not discriminant from a geometric point of view. In the experiment we present we have taken the final scale equal to $0,3$ which seems a reasonable choice, however we have not studied how to optimize the choice of the final scale and we have not tested different final scales.

In figure 3, we present the evolution of $I^{S_0}_{(1,-1,1)}(\tilde{t})$ for the shapes of figure 2. First, we notice that the similarity invariant is very well preserved because the graphs of the similarity equivalent shapes evolves very close each other. We observe that at the initial scales the pixel noise introduced in the discrete representation of the synthetic shapes produces some perturbations in the isoperimetric ratio estimation, however, we can realize that when we

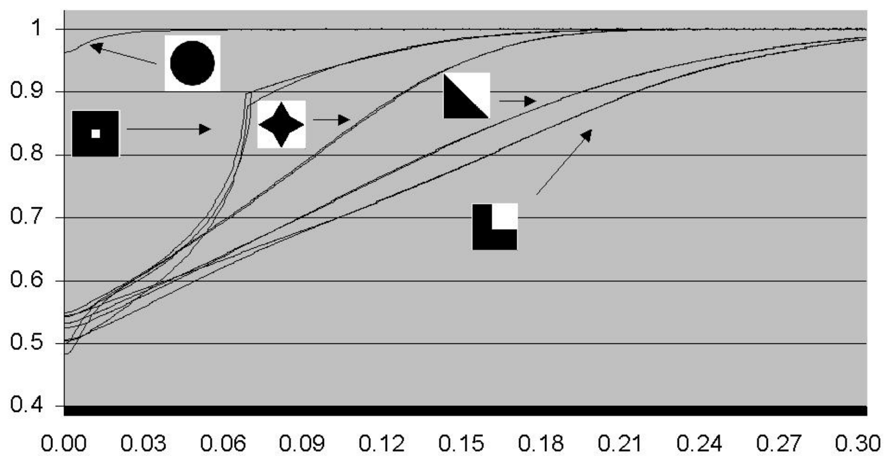

Figure 3: Evolution of $I^{S_0}_{(1,-1,1)}(\tilde{t})$ for the shapes of figure 2.

move across the scales these initial perturbations disappear which is a very good behavior. We can also realize that we can discriminate very well between the different shapes following the isoperimetric ratio evolution. We can observe that the isoperimetric ratio of the shapes converges to 1 as it was shown in [14] We notice that shapes $7-8-9$ have similar evolutions because the evolution of $I^{S_0}_{(1,-1,1)}(\tilde{t})$ is not altered by the location of the inside square. We can observe that, since the curvature of the contour of the hole goes to infinity at the scale where the hole vanishes, a singularity (a point where the evolution is not smooth) appears at such scale. In fact, in some way, we could "characterize" the holes of the shapes following the singularities of the isoperimetric ratio evolution, but the studying of such behavior is beyond the scope of this paper.

In figure 4, we present the evolution of $I^{S_0}_{(1,0,1)}(\tilde{t})$ for the shapes of figure 2. We notice that in this case, shapes 7 and 9 have different evolution following the location of the inside square. This behavior is illustrated in figure 5 where we show some steps of the evolution of $S_{(1,0,1)}(t)$ across the scales for shape 7 and 9. We observe that shape 7 splits in 4 different shapes when the exterior contour touches the inside square. For shape 9 we observe that a singularity in the isoperimetric ratio evolution appears at the scale where the exterior contour touches the inside square and the hole disappears (two boundary curves become a single one). On the other hand, looking at the evolution of shapes $7, 8$ we can observe that in this case the isoperimetric ratio does not converge to 1 as in the case of the mean curvature motion evolution.

In figure 6, we present the evolution of $I^{S_0}_{(1,-1,0)}(\tilde{t})$ for the shapes of figure 2. In the appendix we will show that the asymptotic state of the shape for this multiscale analysis is the convex-hull of the initial shape, so, in particular, the isoperimetric ratio converges towards the isoperimetric ratio of the convex-hull of the shape.

Next, we will present some experiments for the scale normalized area ratio evolution $AR^{S_0}_{(\frac{1}{3},\beta_{-1},\beta_1)}(\tilde{t})$. In this case, we want to discriminate shapes following general affine transformations, so we will use a synthetic shape database composed by affine equivalent shapes. This collection of synthetic shapes is presented in figure 7. For each shape we have evaluated an affine transformation where we have changed the horizontal and vertical sizes in a

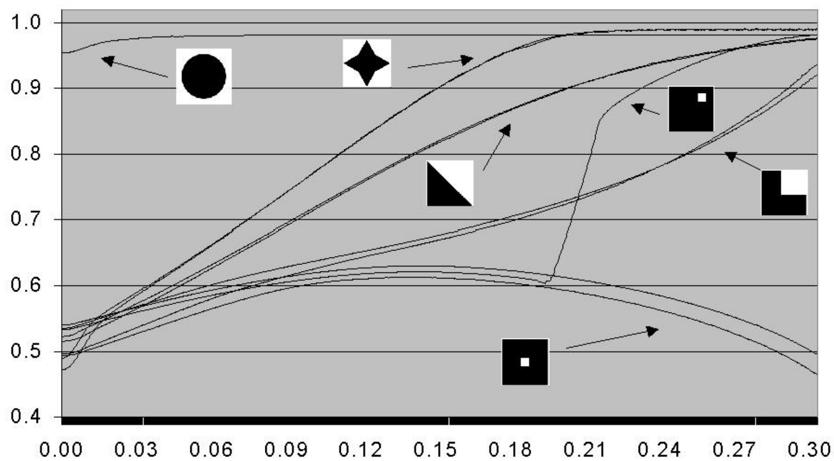

Figure 4: Evolution of $I^{S_0}_{(1,0,1)}(\tilde{t})$ for the shapes of figure 2.

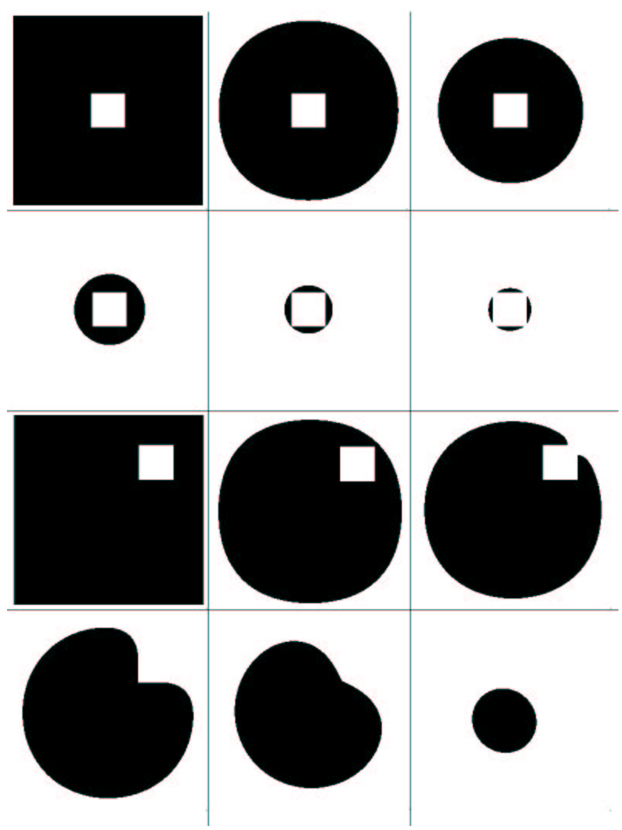

Figure 5: From left to right and from top to down: Evolution of $S_{(1,0,1)}(\tilde{t})$ for shapes 7 and 9 of figure 2.

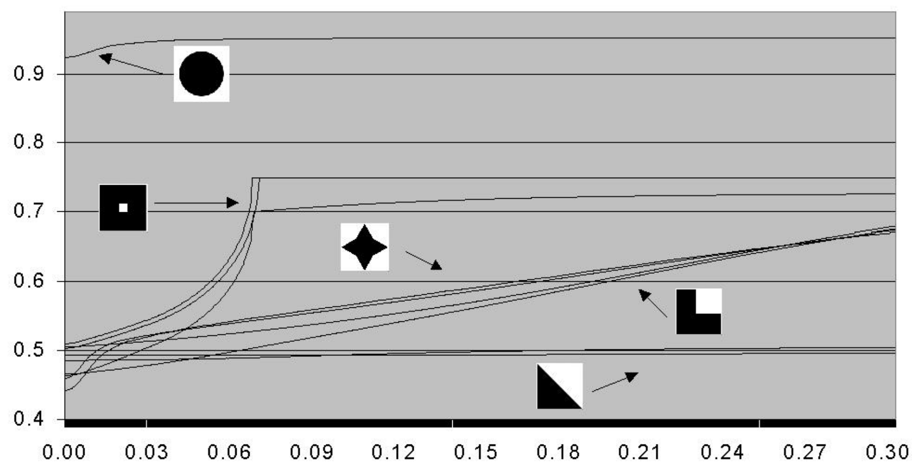

Figure 6: Evolution of $I^{S_0}_{(1,-1,0)}(\tilde{t})$ for the shapes of figure 2.

different way. So shapes $1-2$, $3-4$, $4-5$, $5-6$, $7-8$ and $9-10$ are equivalent modulus an affine transformation. We will compare $AR^{S_0}_{(\frac{1}{3},\beta_{-1},\beta_1)}(\tilde{t})$ for the different shape for $\tilde{t} \in [0, 0.3]$.

In figure 8, we present the evolution of $AR^{S_0}_{(\frac{1}{3},-1,1)}(\tilde{t})$ for the shapes of figure 7. Each shape has associated two graphs which correspond to the evolution of $AR^{S_0}_{(\frac{1}{3},-1,1)}(\tilde{t})$ for the different transformations of the shape. We can observe that initially the area ratio is always equal to 1 and it decreases across the scales. We note that the affine invariance of the multiscale analysis is very well preserved, it means that the evolution of two affine equivalent shapes go so close that most of the time seems to be a single graph in figure 8.

In figure 9, we present the evolution of $AR^{S_0}_{(\frac{1}{3},0,1)}(\tilde{t})$ for the shapes of figure 7. We notice that in this case, only the convex region of the shape evolves, so this behavior produces a strong discrimination between the evolution of shapes following the geometry of their convex and concave regions. This effect can be observed if we compare the evolution of shapes 3 and 7. The evolution of $AR^{S_0}_{(\frac{1}{3},0,1)}(\tilde{t})$ for these two shapes is very different, but the evolution of $AR^{S_0}_{(\frac{1}{3},-1,1)}(\tilde{t})$ for the same shapes are much more similar. So in practice, it means that using the information of the area evolution with different values of β_{-1} and β_1 we obtain a better discrimination power between different shapes.

In figure 10, we present the evolution of $AR^{S_0}_{(\frac{1}{3},-1,0)}(\tilde{t})$ for the shapes of figure 7. The evolution with the multiscale analysis $T_t^{(\frac{1}{3},-1,0)}$ is more sensitive to pixel noise than the ones corresponding to $\beta_1 > 0$. The reason is that in this case we do not have a regularization effect on the boundary. For instance the evolution of the triangles given by shapes 5 and 6 are quite different because of some pixel errors introduced by the application of the affine transformation to shape 5. The regularization effect on the boundary is a well-known property of the morphological multiscale analysis, it means that the multiscale analysis smooths the contours, by lowering the curvature value (see for instance [5], [6] for more details).

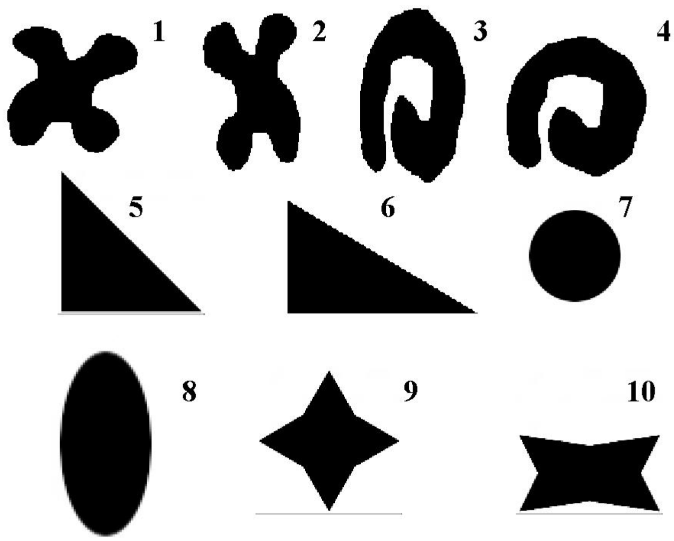

Figure 7: Test shapes used to evaluate the affine invariant scale-normalized area ratio evolution

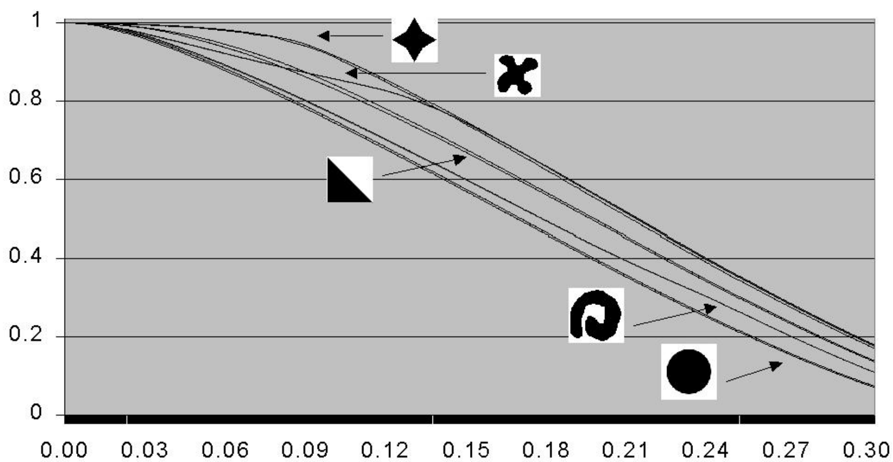

Figure 8: Evolution of $AR^{S_0}_{(\frac{1}{3},-1,1)}(\tilde{t})$ for the shapes of figure 7.

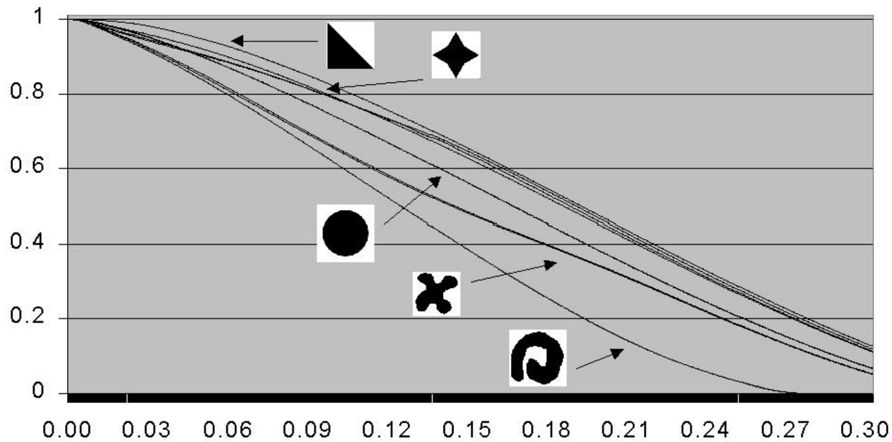

Figure 9: Evolution of $AR^{S_0}_{(\frac{1}{3},0,1)}(\tilde{t})$ for the shapes of figure 7.

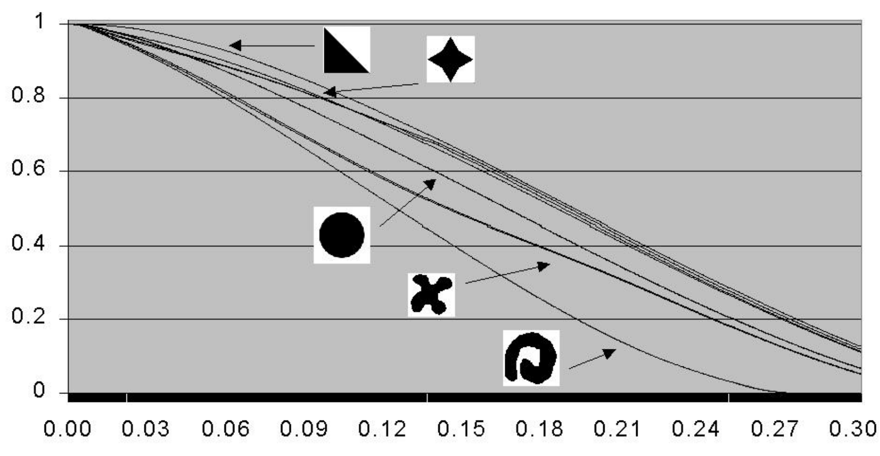

Figure 10: Evolution of $AR^{S_0}_{(\frac{1}{3},-1,0)}(\tilde{t})$ for the shapes of figure 7.

6 Application to shape classification

In this section we apply the techniques we have developed to the problem of shape classification. We use a real shape database developed at Surrey University (see [23] and [24] for more details). We have selected about 200 shapes in this database, in order to introduce some real noise in the shape representation, we have printed, rotated and scanned some of the shapes and we have added them to the database, in figure 11 we present such shape database. We notice that in figure 11 we have normalized the size of the shapes in order to be included in a single image, that is, the relation between the real size of the shapes could be much more different that it appears in figure 11.

The problem we deal with is that, given a shape, we want to find the most similar ones in the database following some distance criterium based on our shape representation. So, first we have to define such distance criterium. In the case of the Euclidean shape representation and given a similarity invariant multiscale analysis, we define the associated Euclidean distance between 2 shapes S_0 and S_0' by the expression

$$d_e^{(p,\beta_{-1},\beta_1)}(S_0, S_0') = \int_0^{\tilde{t}_f} \left| I^{S_0}_{(p,\beta_{-1},\beta_1)}(\tilde{t}) - I^{S_0'}_{(p,\beta_{-1},\beta_1)}(\tilde{t}) \right| d\tilde{t}, \tag{19}$$

where $\tilde{t}_f$ represents the final scale we use to compute the multiscale analysis evolution. In what follows, in the numerical experiments we present for the Euclidean invariant representation, we fit, as in the previous section, $p = 1$ and $\tilde{t}_f = 0.3$

Of course, we can also combine the information of several multiscale analyses to get a more powerful discrimination behavior. In fact, for the Euclidean shape representation, we use

$$d_e(S_0, S_0') = d_e^{(1,-1,1)}(S_0, S_0') + d_e^{(1,0,1}(S_0, S_0') + d_e^{(1,-1,0)}(S_0, S_0'). \tag{20}$$

We notice that with this combination we recover the histogram inversion invariance. That is $d_e(S_0, S_0')$ is invariant under the grey-level image transformation $f \to -f$.

In the case of the affine invariant shape representation we define an affine distance in a similar way

$$d_a^{(\frac{1}{3},\beta_{-1},\beta_1)}(S_0, S_0') = \int_0^{\tilde{t}_f} \left| AR^{S_0}_{(\frac{1}{3},\beta_{-1},\beta_1)}(\tilde{t}) - AR^{S_0'}_{(\frac{1}{3},\beta_{-1},\beta_1)}(\tilde{t}) \right| d\tilde{t}. \tag{21}$$

Again, we can also combine the information of several multiscale analyses to get a more powerful discrimination behavior and we will also use as affine invariant distance criterium :

$$d_a(S_0, S_0') = d_a^{(\frac{1}{3},-1,1)}(S_0, S_0') + d_a^{(\frac{1}{3},0,1)}(S_0, S_0') + d_a^{(\frac{1}{3},-1,0)}(S_0, S_0'). \tag{22}$$

In figure 12 we present a numerical experiment where we have taken 16 shapes in the database and we have estimated the 6 most similar ones ordered by the Euclidean distance criterium $d_e^{(1,-1,1)}(S_0, S_0')$, the results are shown in 2 rows. We notice that for each one of these shapes we have included a new one in the database by printing, rotating and scanning the shape, it is produce a new "noisy" similarity equivalent shape. In figure 12 we observe that in 14 shapes, the most similar one is the noisy version of the shape we have included. In the shapes 2 and 8 (from top to down) of the second row the distance criterium does not provided the noisy version as the closer one. In the case of shape 8 the reason is that there are other shapes in the database that are very similar to the original ones but in the shape 2 the

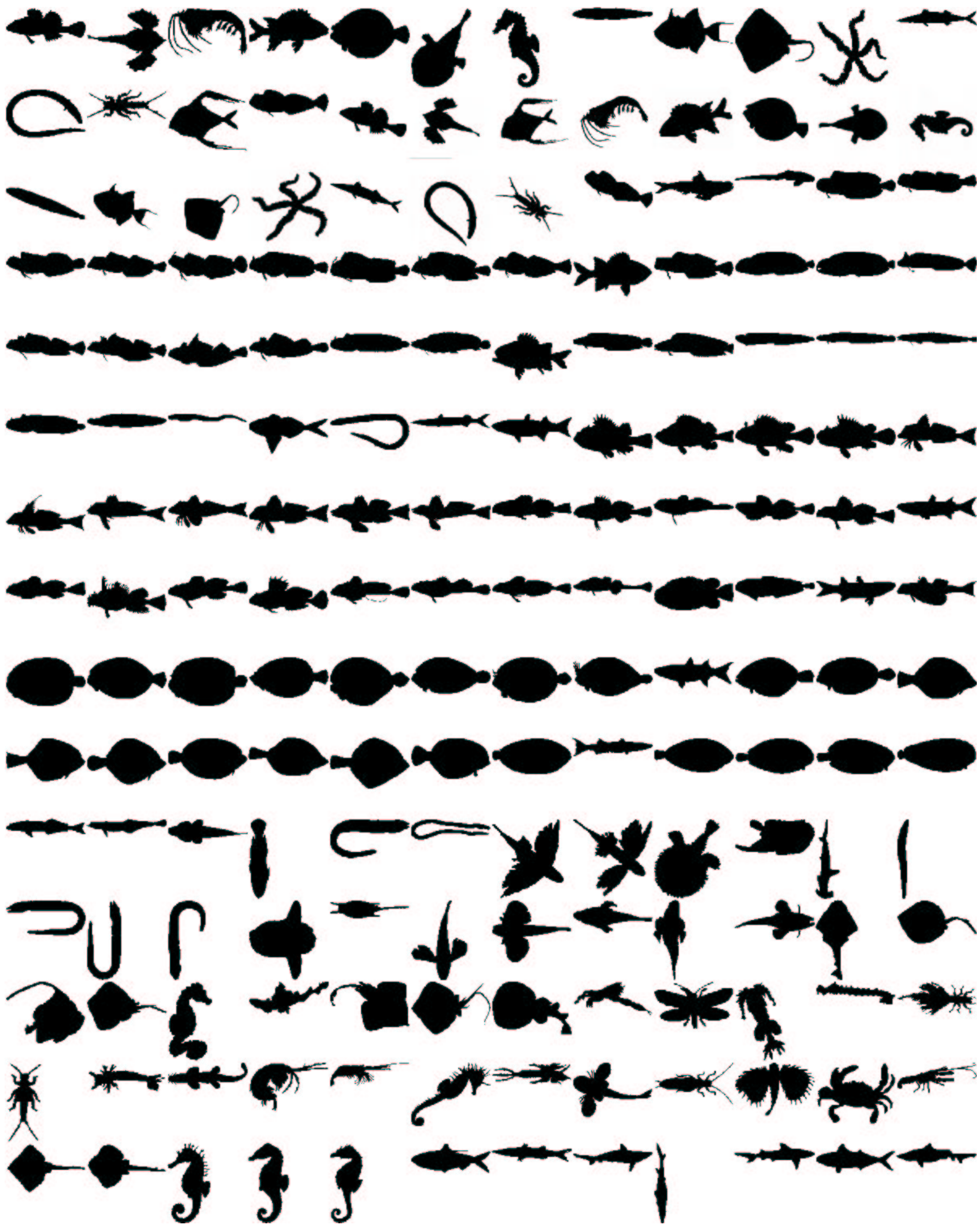

Figure 11: Sea animal shape database taken from the Surrey University real database, where we have included some new ones obtained by printing, rotating and scanning shapes from the database

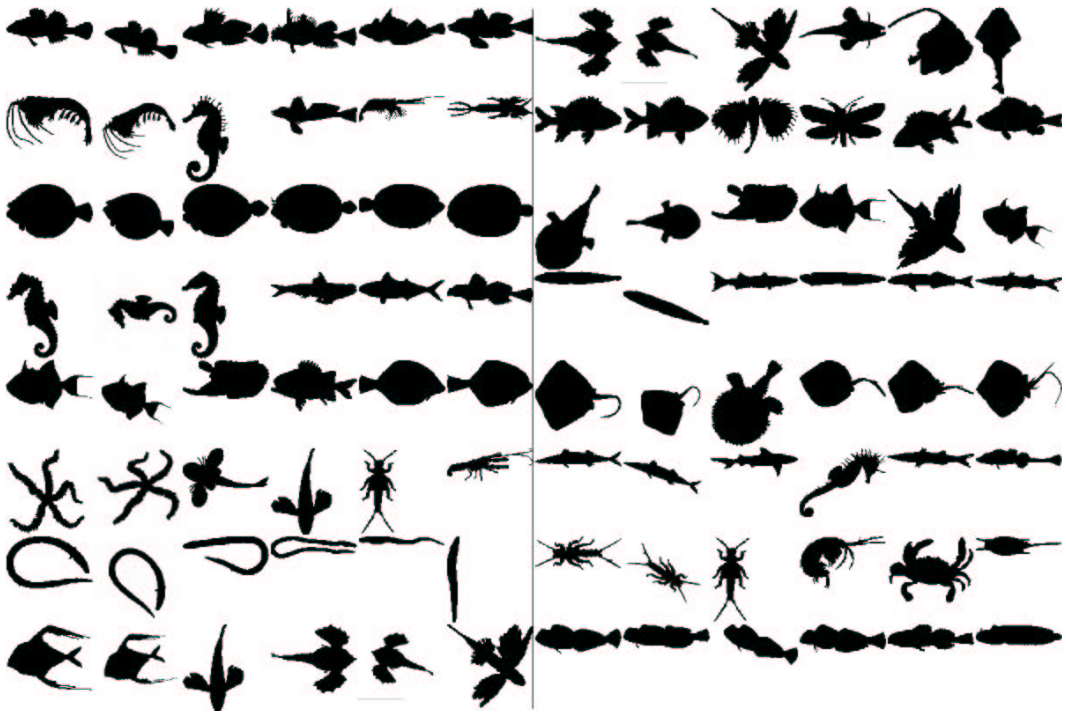

Figure 12: For 16 shapes of the database, and from left to right, we present the 6 most similar ones in the database ordered by the distance criterium $d_e^{(1,-1,1)}(S_0, S_0')$

technique fails and it provides wrong results in the sense that some shapes which have a geometry very different to the original have a distance lower value than the noisy version of the shape included in the database. That's in fact, the reason we need to combine several multiscale analyses to get a more robust and discriminant information.

In figure 13 we present a numerical experiment where we have taken 16 shapes in the database and we have estimated the 6 most similar ones ordered by the Euclidean distance criterium $d_e^{(1,0,1)(S_0,S_0')}(S_0, S_0')$. In this case there is a single shape (shape 8 of second row) where the most similar one is not the noisy version included in the database. The result for shape 2 of the second row seems to be more reasonable, from a perceptual point of view, than in the previous experiment.

In figure 14 we present a numerical experiment where we have taken 16 shapes in the database and we have estimated the 6 most similar ones ordered by the Euclidean distance criterium $d_e^{(1,0,1)}(S_0, S_0')$. In this case, we obtain, in some cases, unexpected combination of shapes like in the case of shape 4 of the first row or shape 8 in the second row. Anyway we obtain that the noisy version included in the database is always the most similar one (except in the shape 8 of the second row).

In figure 15 we present a numerical experiment where we have taken 16 shapes in the database and we have estimated the 6 most similar ones ordered by the Euclidean distance criterium $d_e(S_0, S_0')$ where we have combined 3 multiscale analyses. We notice that, in general, the classification is pretty good from a perceptual point of view. In table 1 we present the values of the distance criterium $d_e(S_0, S_0')$ for the numerical experiment of figure 15. We observe that for shape 8 of the second row, the only case where the method fails in the sense that the most similar shape is not the noisy version included in the database,

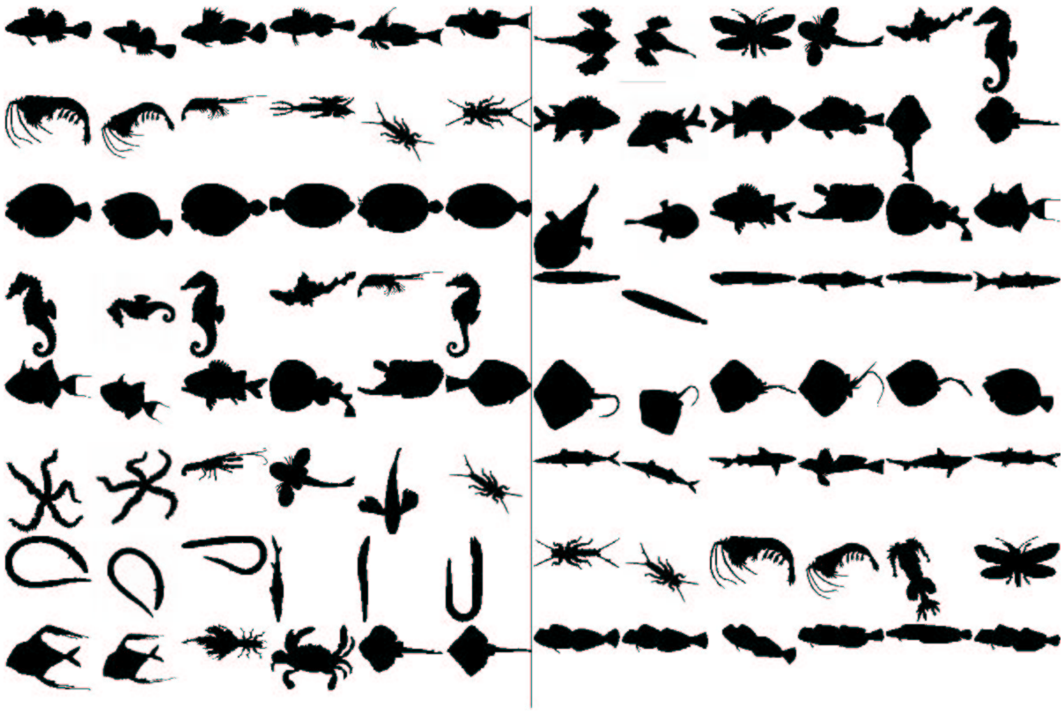

Figure 13: For 16 shapes of the database, and from left to right, we present the 6 most similar ordered by the distance criterium $d_e^{(1,0,1)}(S_0, S'_0)$

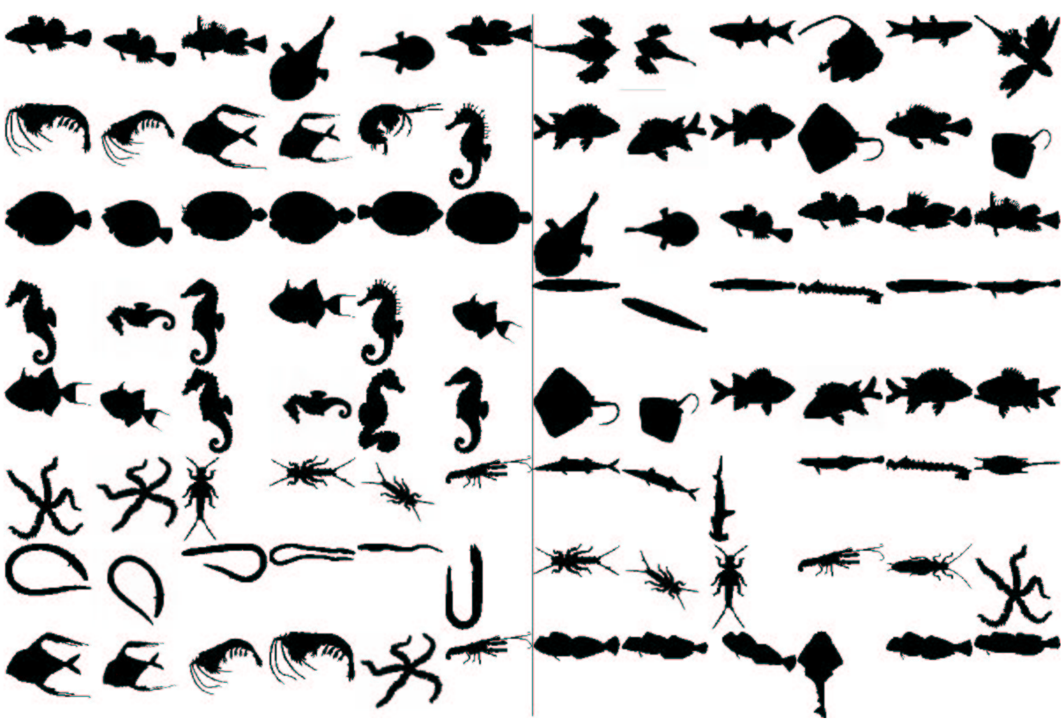

Figure 14: For 16 shapes of the database, and from left to right, we present the 6 most similar ordered by the distance criterium $d_e^{(1,-1,0)}(S_0, S'_0)$

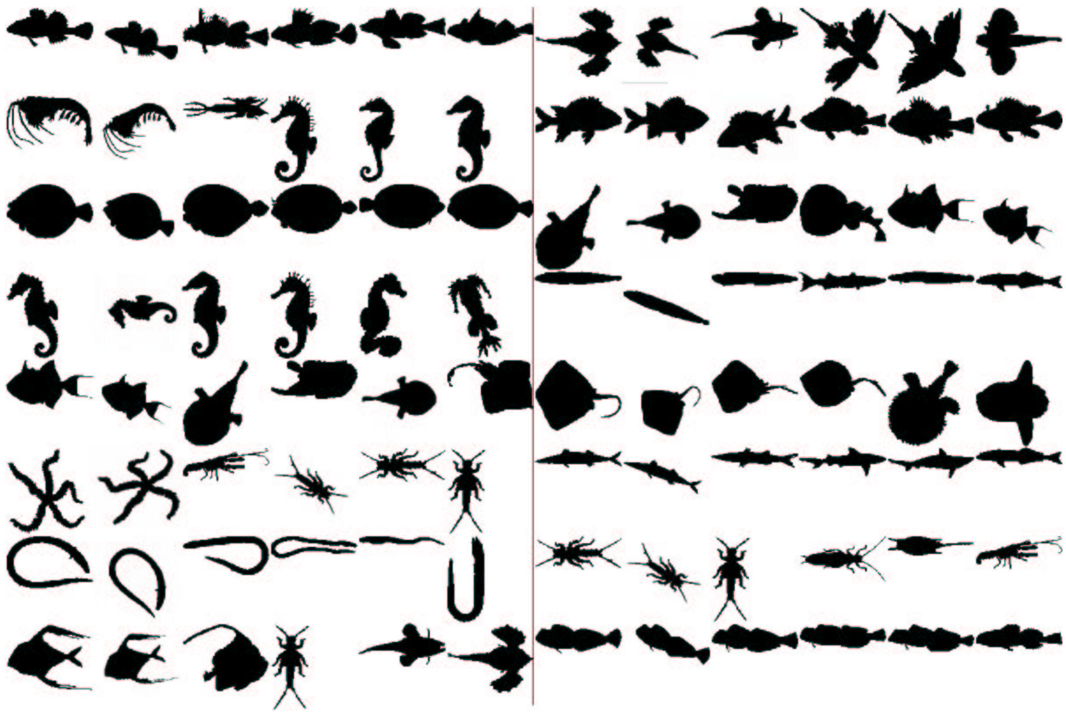

Figure 15: For 16 shapes of the database, and from left to right, we present the 6 most similar ordered by the distance criterium $d_e(S_0, S'_0)$

the shapes are very similar and the distance values are very low. We also notice that when there are not similar shapes in the database to the one we want to classify, there are a big difference in the distance value between the noisy version of the shape and the most similar one in the database, that is the case for shapes $2, 5, 6, 7, 8$ in the first row.

Next, we present some experimental results concerning the affine invariant classification. To simplify the exposition we will give directly the results obtained with the combination of the 3 associated multiscale analyses. In figure 16 we present a numerical experiment where we have taken 16 shapes in the database and we have estimated the 6 most similar ones ordered by the affine distance criterium $d_a(S_0, S'_0)$. First we observe that we are classifying the shapes from an affine point of view, and a general affine transformation can modify the geometry of a shape in a strong way. For instance, in the shape 4 of the second row, the original shape and the third most similar one (in terms the affine distance) are, in fact, very similar from an affine point of view (we have just to expand the vertical axis to go from one shape to the other one). In other words, the affine classification could not be the best one from a human perception point of view. In any case the results are pretty good, we obtain that in 12 shapes, the method find out that the most similar one is the noisy version included in the database, in shapes 3 of the first row and $2, 8$ of the second row there are another shapes in the database which are very similar. The method seems to fail for shape 4 of second row where the noisy version does not appear between the 6 most similar ones. The reason, as it is shown at table 2 where we present the values of the distance criterium $d_a(S_0, S'_0)$ for this experiment, is that from the point of view of affine transformations, the distance between this shape and the proposed ones is very low.

Remark (noise robustness) In this paper we have not focussed our attention in improving

Table 1: We show, for the experiment in figure 15, the values of the distance function $d_e(S_0, S'_0)$

0.0	1.1-02	5.4-02	5.7-02	7.7-02	1.1-01	0.0	9.7-03	1.0-01	1.1-01	1.6-01	1.7-01
0.0	3.3-02	2.0-01	2.0-01	2.2-01	2.3-01	0.0	2.2-02	2.7-02	8.0-02	1.0-01	1.1-01
0.0	5.2-03	3.8-02	4.8-02	8.4-02	1.1-01	0.0	1.9-02	8.0-02	1.1-01	1.2-01	1.3-01
0.0	1.4-02	2.6-02	1.1-01	1.2-01	1.2-01	0.0	2.3-02	5.4-02	8.6-02	8.7-02	8.7-02
0.0	1.3-02	1.2-01	1.2-01	1.2-01	1.5-01	0.0	2.1-02	1.4-01	1.4-01	1.8-01	1.8-01
0.0	2.1-02	2.6-01	3.0-01	3.1-01	3.2-01	0.0	1.5-02	7.0-02	7.2-02	1.1-01	1.1-01
0.0	2.3-02	1.1-01	2.4-01	3.0-01	3.4-01	0.0	2.7-02	8.9-02	2.0-01	2.5-01	2.5-01
0.0	4.0-02	2.5-01	2.7-01	2.7-01	2.9-01	0.0	1.7-02	2.7-02	2.8-02	3.8-02	7.6-02

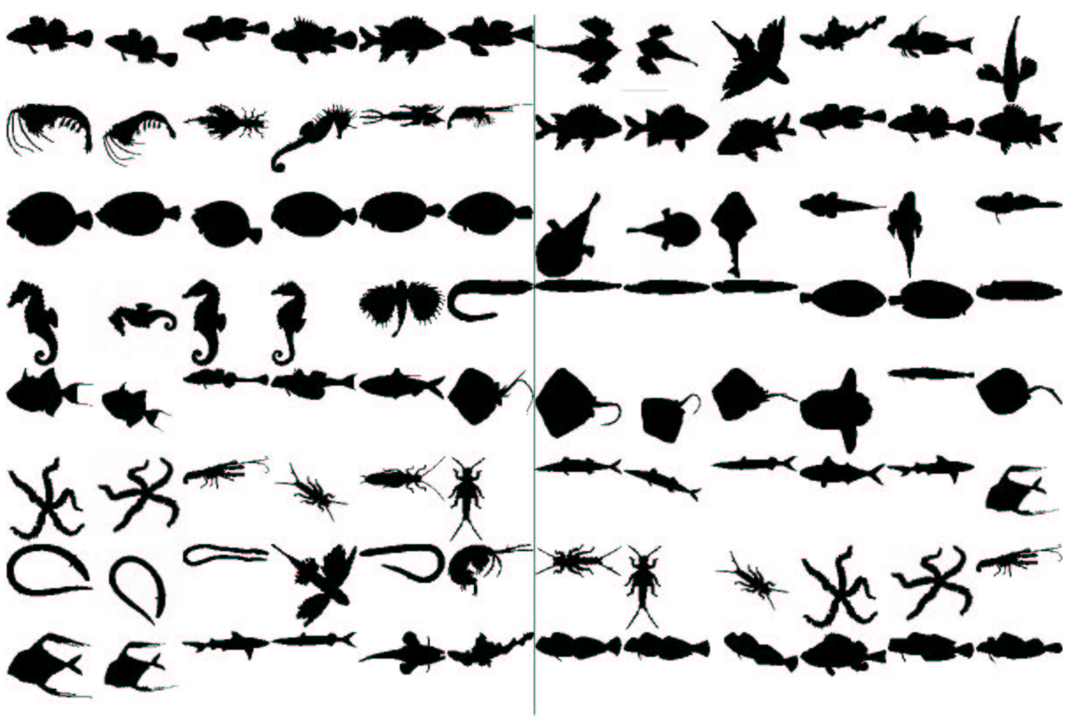

Figure 16: From left to right, we show for 16 shapes of the database the 6 most similar ones ordered by the distance criterium $d_a(S_0, S'_0)$

Table 2: We show, for the experiment in figure 16, the values of the distance function $d_a(S_0, S_0')$

0.0	1.3-02	2.6-02	3.0-02	3.4-02	3.5-02	0.0	2.4-02	2.8-02	2.9-02	6.2-02	6.3-02
0.0	4.4-02	1.1-01	1.4-01	1.4-01	1.8-01	0.0	2.0-02	2.7-02	2.9-02	3.4-02	3.4-02
0.0	4.4-03	1.1-02	1.4-02	1.4-02	2.5-02	0.0	2.5-02	2.9-02	4.3-02	4.4-02	6.4-02
0.0	3.9-02	3.9-02	8.2-02	9.0-02	9.0-02	0.0	3.3-02	3.6-02	3.9-02	4.2-02	4.2-02
0.0	1.9-02	6.7-02	6.8-02	6.8-02	6.9-02	0.0	1.5-02	2.6-02	2.7-02	4.3-02	4.9-02
0.0	8.0-02	2.8-01	3.1-01	3.1-01	3.2-01	0.0	3.4-02	5.7-02	5.7-02	5.8-02	6.7-02
0.0	4.5-02	8.4-02	1.5-01	1.5-01	1.8-01	0.0	1.2-01	1.7-01	3.3-01	3.5-01	4.0-01
0.0	2.6-02	6.5-02	7.5e-02	8.2-02	8.3-02	0.0	1.8-02	1.9-02	2.1-02	2.3-02	2.9-02

the noise robustness of our analysis, because in fact, as we can see in the real database experiments, our analysis is rather robust to noise even without specific strategy to improve the noise robustness behavior, however there are rooms for some improvements in this sense that we have not tested: First, we can observe that when β_1 is equal to 0 we have not got the nice regularization behavior of the mean curvature motion equation which removes noise in a very efficient way, we can avoid the case $\beta_1 = 0$ taking as multiscale analysis $(p, \beta_1, \beta_{-1}) = (p, -1, 1), (p, -1, \epsilon), (p, -\epsilon, 1)$ where $\epsilon > 0$ would be a parameter to fit in the applications. Notice that with this choice, we keep the invariance of the analysis under inversion of the histogram of the image (change f by $-f$). Secondly, we can observe in the experiments (see figures 3, 4, 6) that most of the noise is concentrated in the first scales of the evolution, so one way to improve the noise-robustness behavior is to compare the isoperimetric ratio evolution of two shapes not in the interval $[0, \tilde{t}_f]$ but in the interval $[\tilde{t}_0, \tilde{t}_f]$ where $\tilde{t}_0 > 0$ should be a parameter to fit in the applications. We could also weight the influence of the multiscale analysis in the shape comparison, for instance, the mean curvature motion is the multiscale analysis more robust concerning the noise, so we could assign a greater weight to this multiscale analysis in the shape comparison. Finally, we could also estimate the initial area of the shape in a more robust way, indeed, in the case we deal with shapes without holes where the contour is given by a single Jordan curve, then, we know that the area evolution under the action of the mean curvature motion is given by $|S(t)| = |S_0| - 2\pi t$. So we can apply the mean curvature motion to remove noise until a given scale $t_1 > 0$ and then we estimate the initial area of the shape using the formula : $|S_0| = |S(t_1)| + 2\pi t_1$. We have not used all these kind of improvement in the noise robustness behavior of the analysis because we do not wanted to add extra parameters in the experiments which could disturb the interpretation of the results (If you have a lot of parameters to manage is much more difficult to interpret the results). However, as we have pointed out, the numerical results are pretty good even without using any strategy to improve the noise-robustness behavior.

7 Conclusions

In this paper, we have presented a new geometric invariant shape representation using morphological multiscale analyses. The main idea we develop here is that if we take any global invariant of the shape, and we follow the evolution of this invariant under the action of a morphological multiscale analysis, then this evolution is also an invariant of the shape and it provides a much more robust and useful information about the geometry of the shape. In particular, the invariants we analyze in this paper are based on the area and perimeter evolution of the shape under the action of a morphological multiscale analysis.

We have introduced a similarity invariant shape representation based on a scale-normalized isoperimetric ratio evolution. In this case we have focused our attention in the morphological multiscale analysis generated by the mean curvature motion evolution. In order to increase the discrimination power of the shape representation, we propose to combine the information of the evolution of shapes using different values of β_{-1} and β_1. In this way we can discriminate between the convex and concave regions of the shapes. We have presented some numerical experiments and the results are very promising.

In the case of general affine geometric transformations the proposed geometric invariant is based on a scale-normalized evolution of the area using the affine invariant morphological multiscale analysis $T_t^{(\frac{1}{3},\beta_{-1},\beta_1)}$. We have presented some numerical experiments and the results are also very promising.

Acknowledgments. This work has been supported by the European TMR network *Viscosity Solutions and their Applications.* We want to acknowledge the anonymous reviewers for their valuable comments which have improved a lot the paper presentation. We want also to thanks to Prof. Mohktarian at Surrey University who allow us to use the real sea animals database we use in some of our numerical experiments.

8 Appendix

8.1 Area and perimeter evolution.

In this section, we will show propositions 1 and 2 concerning the evolution of the perimeter and area of a shape following the equation (3). The results that we show here are a generalization of the ones presented in [16] for the Euclidean shortening flow which corresponds to the particular choice $\beta(s) = s$. First, we will present some lemma which are a generalization of the ones presented in [16] for the mean curvature equation which corresponds to the particular choice $\beta(s) = s$. We will assume that the evolution of the boundary of the shape, $C(t)$, is a family of simple Jordan curves, and we will denote by $C(t,u) = (x(t,u), y(t,v))$ a parameterization of the curve $C(t)$, we will also use the notation

$$v(t,u) = \left|\frac{\partial C}{\partial u}(t,u)\right| = \sqrt{\left(\frac{\partial x}{\partial u}(t,u)\right)^2 + \left(\frac{\partial y}{\partial u}(t,u)\right)^2}$$

we will assume (without loss of generality) that the interval of definition of u is $[0, 2\pi]$.

Lemma 1

$$\frac{\partial v}{\partial t} = -k\beta(k)v.$$

Proof : We compute

$$\begin{aligned}
\frac{\partial v^2}{\partial t} &= \frac{\partial}{\partial t}\langle\frac{\partial C}{\partial u},\frac{\partial C}{\partial u}\rangle \\
&= 2\langle\frac{\partial C}{\partial u},\frac{\partial^2 C}{\partial t\partial u}\rangle \\
&= 2\langle\frac{\partial C}{\partial u},\frac{\partial^2 C}{\partial u\partial t}\rangle \\
&= 2\langle\frac{\partial C}{\partial u},\frac{\partial}{\partial u}(\beta(k)\vec{N})\rangle \\
&= 2\langle\frac{\partial C}{\partial u},\frac{\partial \beta(k)}{\partial u}\vec{N} - vk\beta(k)\vec{T}\rangle
\end{aligned}$$

using the Frenet equation $\frac{\partial \vec{N}}{\partial u} = -vk\vec{T}$. Since $\frac{\partial C}{\partial u} = v\vec{T}$, we have

$$\begin{aligned}
\frac{\partial v^2}{\partial t} &= 2\langle v\vec{T},\frac{\partial \beta(k)}{\partial u}\vec{N} - vk\beta(k)\vec{T}\rangle \\
&= -2v^2k\beta(k)
\end{aligned}$$

Hence we deduce $\frac{\partial v}{\partial t} = -vk\beta(k)$.

Lemma 2

$$\frac{\partial \vec{N}}{\partial t} = -\frac{\partial \beta(k)}{\partial s}\vec{T}.$$

where s is the arclength parameterization.

Proof of lemma: First, we compute the derivative of $\vec{T}$

$$\begin{aligned}
\frac{\partial \vec{T}}{\partial t} &= \frac{\partial}{\partial t}(\frac{1}{v}\frac{\partial C}{\partial u}) \\
&= \frac{\partial}{\partial t}(\frac{1}{v})\frac{\partial C}{\partial u} + \frac{1}{v}\frac{\partial^2 C}{\partial t\partial u} \\
&= -\frac{1}{v^2}\frac{\partial v}{\partial t}\frac{\partial C}{\partial u} + \frac{1}{v}\frac{\partial^2 C}{\partial u\partial t} \\
&= \frac{1}{v^2}k\beta(k)v\frac{\partial C}{\partial u} + \frac{1}{v}\frac{\partial}{\partial u}(\beta(k)\vec{N}) \\
&= k\beta(k)\vec{T} + \frac{1}{v}\frac{\partial \beta(k)}{\partial u}\vec{N} + \frac{1}{v}\beta(k)\frac{\partial \vec{N}}{\partial u} \\
&= k\beta(k)\vec{T} + \frac{1}{v}\frac{\partial \beta(k)}{\partial u}\vec{N} - \frac{1}{v}\beta(k)vk\vec{T} \text{ (by Frenet eq.)} \\
&= \frac{1}{v}\frac{\partial \beta(k)}{\partial u}\vec{N} \\
&= \frac{\partial \beta(k)}{\partial s}\vec{N}.
\end{aligned}$$

on the other hand, since $\langle \vec{N}, \vec{N} \rangle = 1$ and $\langle \vec{T}, \vec{N} \rangle = 0$ we have

$$\langle \frac{\partial \vec{N}}{\partial t}, \vec{N} \rangle = 0$$
$$\langle \frac{\partial \vec{T}}{\partial t}, \vec{N} \rangle + \langle \vec{T}, \frac{\partial \vec{N}}{\partial t} \rangle = 0$$

therefore using the previous estimations we conclude the proof of the lemma.

Next, we will present the mathematical proofs of the estimations (5) and (6).

Proof of Proposition 1: Since we have showed above $\frac{\partial v}{\partial t} = -k\beta(k)v$, so if we integrate this equality we obtain

$$\begin{aligned} \frac{\partial |C(t)|}{\partial t} &= \frac{\partial}{\partial t}\left(\int_0^{2\pi} v du\right) = \int_0^{2\pi} \frac{\partial v}{\partial t} du = \\ &= -\int_0^{2\pi} -k\beta(k) v du = -\int_0^{|C(t)|} k\beta(k) ds \end{aligned}$$

Proof of Proposition 2: The area $|S(t)|$ can be written as :

$$|S(t)| = -\int_0^{2\pi} \frac{1}{2}\langle C, v\vec{N} \rangle du$$

Using the previous lemma, we have:

$$\begin{aligned} \frac{\partial |S(t)|}{\partial t} &= -\frac{1}{2}\int_0^{2\pi} v\beta(k) - \langle C, vk\beta(k)\vec{N} \rangle + \langle C, v\frac{\partial \beta(k)}{\partial s}\vec{T} \rangle du \\ &= -\frac{1}{2}\int_0^{2\pi} v\beta(k) - \langle C, vk\beta(k)\vec{N} \rangle - \langle C, \frac{\partial \beta(k)}{\partial u}\vec{T} \rangle du. \end{aligned}$$

We integrate the last term by parts:

$$\begin{aligned} \frac{\partial |S(t)|}{\partial t} &= -\frac{1}{2}\int_0^{2\pi} v\beta(k) - \langle C, vk\beta(k)\vec{N} \rangle + \langle \frac{\partial C}{\partial u}, \beta(k)\vec{T} \rangle + \langle C, \beta(k)\frac{\partial \vec{T}}{\partial u} \rangle du \\ &= -\frac{1}{2}\int_0^{2\pi} v\beta(k) - \langle C, vk\beta(k)\vec{N} \rangle + \langle v\vec{T}, \beta(k)\vec{T} \rangle + \langle C, \beta(k)vk\vec{N} \rangle du \\ &= -\int_0^{2\pi} v\beta(k) du \\ &= -\int_0^{L} \beta(k) ds. \end{aligned}$$

8.2 Similarity invariant geometric flows.

Next, we are going to show proposition 3 concerning the shape of the similarity invariant multiscale analyses.

Proof of Proposition 3: Since the morphological multiscale analysis (3) are Euclidean invariant, we can assume that the similarity transformation is given by a zoom, that is $H(x, y) = (sx, sy)$. A morphological multiscale analysis, satisfies the similarity invariant principle if and only if for any solution $u(t, x, y)$ of equation (3), the function

$$v(t, x, y) = u(t'(H, t), sx, sy)$$

is also a solution of equation (3). On the other hand
$\frac{\partial v}{\partial t}(t,x,y) = \frac{\partial t'(H,t)}{\partial t}\frac{\partial u}{\partial t}(t'(H,t),sx,sy) = \frac{\partial t'(H,t)}{\partial t}\beta(curv(u(t,sx,sy)))\,\|\nabla u(t,sx,sy)\|$
and
$\beta(curv(v(t,x,y)))\,\|\nabla v(t,x,y)\| = \beta(s\cdot curv(u(t,sx,sy)))s\cdot\|\nabla u(t,sx,sy)\|$

Then $v(t,x,y)$ is solution of (3) iff for any w

$$\frac{\partial t'(H,t)}{\partial t}\beta(w) = s\beta(sw) \tag{23}$$

First, we consider the case $w \geq 0$. We notice that if $\beta(1)=0$ then by the above equality $\beta(s)=0$ for any $s>0$ and the result is trivial. In the case $\beta(1)\neq 0$, since $\frac{\partial t'(H,t)}{\partial t}$ can not depends on w, then:

$$\frac{\partial t'(H,t)}{\partial t} = s\frac{\beta(s)}{\beta(1)} \tag{24}$$

and therefore

$$t'(H,t) = s\frac{\beta(s)}{\beta(1)}t. \tag{25}$$

using equalities (23) and (24) we obtain that

$$\beta(s)\beta(w) = \beta(1)\beta(sw) \quad for\ any\ s>0,\ w\in R$$

if we take logarithms in this equality, and we compute the derivatives with respect to w, and we evaluate it in $w=1$, we obtain:

$$\frac{\beta'(1)}{\beta(1)}\frac{1}{s} = \frac{\beta'(s)}{\beta(s)}$$

therefore, if we integrate this equality, we obtain that

$$\beta(s) = \beta(1)s^{\frac{\beta'(1)}{\beta(1)}} for\ any\ s>0$$

then we conclude (23) taking

$$p = \frac{\beta'(1)}{\beta(1)}$$

Moreover using (25) and the previous equality we obtain:

$$t'(H,t) = s^{p+1}t$$

Now, we consider the case $w<0$. In the same way, we obtain that if $\beta(-1)=0$ the $\beta(-s)=0$ for any $s>0$ and the result is trivial, in the case $\beta(-1)\neq 0$, we obtain that

$$\beta(-s) = \beta(-1)s^{\frac{-\beta'(-1)}{\beta(-1)}} for\ any\ s>0$$

and

$$t'(H,t) = s^{\frac{-\beta'(-1)}{\beta(-1)}+1}t$$

Therefore if $\beta(1)\beta(-1)\neq 0$ since $t'(H,t)$ does not depends on the sign of w we have that

$$p = \frac{\beta'(1)}{\beta(1)} = \frac{-\beta'(-1)}{\beta(-1)}$$

which concludes the proof.

Next we show a closed-form expression for the evolution of a circle under the action of a similarity invariant morphological multiscale analysis.

Lemma 3 *If* $S_0 = B_{R_0}(x_0, y_0)$ *is a circle of radius* R_0*,and* $T_t^{(p,\beta_{-1},\beta_1)}$ *is a similarity invariant morphological multiscale analysis, then,* $S(t) = B_{R(t)}(x_0, y_0)$ *where* $R(t)$ *is given by*

$$R(t) = \left(R_0^{p+1} - \beta_1(p+1)t\right)_+^{\frac{1}{p+1}}$$

Proof: Using the equivalence with the curve evolution, we have that the radius $R(t)$ of the circle satisfies the equation :

$$\frac{\partial R}{\partial t}(t) = -\beta_1 \left(\frac{1}{R(t)}\right)^p$$

and the solution of this equation is given by

$$R(t) = \begin{cases} \left(R_0^{p+1} - \beta_1(p+1)t\right)^{\frac{1}{p+1}} & if \quad t \leq \frac{R_0^{p+1}}{\beta_1(p+1)} \\ 0 & if \quad t > \frac{R_0^{p+1}}{\beta_1(p+1)} \end{cases}$$

which concludes the proof.

9 Viscosity solutions

The proper framework to study the multiscale operator is the theory of viscosity solution (cf. [3]); we refer the reader to the "user's guide" [10] and the references inside.

Here we just want to make some remarks because the equation (3) with (8) has a possible difficulty for $Du = 0$.

For $|Du| \neq 0$, we may write:

$$\begin{aligned} curv(u) &= div(\frac{Du}{|Du|}) \\ &= \frac{1}{|Du|}(\Delta u - \frac{1}{|Du|^2}\sum_{i=1}^{2}\frac{\partial^2 u}{\partial x_i^2}(\frac{\partial u}{\partial x_i})^2) \\ &= \frac{1}{|Du|}Tr((Id - \frac{Du \otimes Du}{|Du|^2})D^2u) \end{aligned}$$

with $q \otimes q = (q_i q_j)_{i,j}$ and Tr the trace operator.

The well-know mean curvature operator is

$$F(q, X) = Tr((Id - \frac{q \otimes q}{|q|^2})X).$$

Then the operator of (3) with (8) is

$$G(q, X) = \begin{cases} \beta(1)(F(q, X))^p |q|^{1-p} & \text{if } F(q, X) \geq 0, \\ \\ \beta(-1)(-F(q, X))^p |q|^{1-p} & \text{if } F(q, X) \leq 0. \end{cases}$$

The extensions of F to $(0, X)$ is given by (cf. user's guide)

$$\underline{F}(q, X) = \begin{cases} F(q, X) & \text{if } q \neq 0, \\ \\ -2||X|| & \text{if } q = 0, \end{cases} \qquad \bar{F}(q, X) = \begin{cases} F(q, X) & \text{if } q \neq 0, \\ \\ 2||X|| & \text{if } q = 0. \end{cases}$$

Then the extension of G is

$$\underline{G}(q,X) = \begin{cases} G(q,X) & \text{if } q \neq 0, \\ \begin{cases} 0 & \text{if } p < 1, \\ -2||X|| & \text{if } p = 1, \\ -\infty & \text{if } p > 1, \end{cases} & \text{if } q = 0, \end{cases}$$

$$\bar{G}(q,X) = \begin{cases} G(q,X) & \text{if } q \neq 0, \\ \begin{cases} 0 & \text{if } p < 1, \\ 2||X|| & \text{if } p = 1, \\ +\infty & \text{if } p > 1, \end{cases} & \text{if } q = 0. \end{cases}$$

Hence, for $p \in [0,1]$, the operator G has a upper and lower envelope bounded. In particular, for $p \in [0,1]$, we have

$$\bar{G}(0,0) = \underline{G}(0,0). \tag{26}$$

The case $p > 1$ need new definition of viscosity solutions ([19] for example).

The operator F is degenerate elliptic, i.e.,

$$F(X,q) \geq F(Y,q) \quad \text{if } X \geq Y, \tag{27}$$

for all $q \in I\!R^2$, $X, Y \in \mathcal{S}^2$ where $\mathcal{S}^2$ is the set of symmetric matrix. Then G is degenerate elliptic too.

Moreover the operator F is geometric, i.e.,

$$F(\lambda X + \mu(q \otimes q)), \lambda q) = \lambda F(X,q) \quad \text{for all } \lambda > 0 \text{ and } \mu \in I\!R. \tag{28}$$

It is straightforward that the operator G satisfies the same property.

With these three properties, we have the two following results taken from [29].

Proposition 4 *Assume (26), (27) and (28). If $u \in UC(I\!R^2)$ where UC denotes the space of uniformly continuous function, is a subsolution of (3) and v is a discontinuous supersolution of (3), and $u(.,0) \leq v(.,0)$ on $I\!R^2 \times \{0\}$ then $u(.,t) \leq v(.,t)$ on $I\!R^2$ for all $t > 0$.*

Proposition 5 *Assume (26), (27) and (28). Then, for any $u_0 \in UC(I\!R^2)$,there exists a unique solution $u \in UC(I\!R^2)$ of the equation.*

Remark. We can apply the above proposition to the similarity invariant multiscale analysis 3 and we obtain that for $p \leq 1$ $\beta(1) \geq 0$ and $\beta(-1) \leq 0$) the problem is well-posed in the framework of the uniformly continuous functions.

Using these two results, we can, for example, obtain a solution for the evolution of a disk. We approximate the discontinuous initial function u_0 by a decreasing sequence of regular functions u_0^n in $UC(I\!R^2)$. Then there exists an unique solution u^n associated to each initial data u_0^n. Using the regularity properties of viscosity solutions, the upper star limit sup of the sequence of solutions, i.e., $\limsup_{n\to+\infty,y\to x} u^n$, is a subsolution of the equation. And the lower star limit inf ($\liminf_{n\to+\infty,y\to x} u^n$) is a supersolution. But, the functions u^n are continuous and the sequence $(u^n)_n$ is decreasing. Then $\limsup_{n\to+\infty,y\to x} u^n = \inf_n u^n$ and $\liminf_{n\to+\infty,y\to x} u^n = (\inf_n u^n)_*$ Hence $u = \inf_n u^n$ is a solution of the problem.

Another interesting approach to the viscosity solutions for the morphological multiscale analyses have been proposed in [18] where they use iterated contrast invariant operators to approximate the solution.

Concave transformation

Proposition 6 *Let S be a convex set. We consider the problem:*

$$\begin{cases} \dfrac{\partial u}{\partial t} = -(-(curv(u))_-)^p|Du| & in\ I\!R^2 \times I\!R^+, \\ u = 1\!\!1_{\{I\!R^2 \setminus S\}} & on\ I\!R^2 \times \{0\}, \end{cases} \tag{29}$$

($\beta(1) = 0$ and $\beta(-1) = -1$ in the definition (8)) where the function $1\!\!1_{\{I\!R^2\setminus S\}}$ is the characteristic function of the complementary set of S.

Then the stationary function $u(x,t) = 1\!\!1_{\{I\!R^2\setminus S\}}(x)$ is a viscosity solution of (29).

Proof : First we prove the property for the sub-solution.

Let $\varphi \in C^\infty(I\!R^2 \times I\!R^+)$ and (x_0,t_0) a maximum point of $u^* - \varphi$ in $I\!R^2 \times I\!R^+_*$. We may assume that $u^*(x_0,t_0) = \varphi(x_0,t_0)$ by adding $u^*(x_0,t_0) - \varphi(x_0,t_0)$ to the test-function φ.

The function u is obviously C^∞ in time variable then, by classical properties of maximum points, we have

$$\frac{\partial u}{\partial t}(x_0,t_0) = \frac{\partial \varphi}{\partial t}(x_0,t_0) = 0.$$

For the same reasons, everywhere the function u is regular at the point (x_0,t_0), the point equation (29) is satisfied by the function-test φ. The case when $D\varphi(x_0,t_0) = 0$ need the use of the theory of discontinuous Hamiltonian (cf. part on viscosity solutions).

It remains the case when x_0 is in the boundary of S, i.e, $x_0 \in \partial S$. Since the curvature of φ appears in the equation, we will investigate the level set of φ associated to the value $\varphi(x_0,t_0)$, i.e., intersection of φ with the plan $z = u^*(x_0,t_0)$, denoted by I. (In fact, we consider only the connect part of I contained (x_0,t_0), still noted I.)

If $|D\varphi(x_0,t_0)| = 0$, then I is a point or a plan around (x_0,t_0) and the equation (29) is satisfied by φ using the same arguments as before.

If $|D\varphi(x_0,t_0)| \neq 0$, then I is a curve. We have two cases following its regularity:

- If, at the point x_0, the set S have a "convex" corner, it is impossible to have a regular function such that $u^* \leq \varphi$. Remark that if the set S has a "concave" corner, it can not be a sub-solution because we are able to construct test-function with non-positive curvature at this corner.

- Then the boundary ∂S has a curvature at the point x_0, we note it $curv(S)(x_0)$. And, since $u^* \leq \varphi$, we get $curv(S)(x_0) \leq curv(\varphi)(x_0)$. Since the set S is convex, $curv(S)(x_0) \geq 0$. Hence

$$\frac{\partial \varphi}{\partial t}(x_0,t_0) = 0 \leq -(-(curv(\varphi(x_0,t_0))_-)^p|D\varphi(x_0,t_0)|$$

and it concludes the case of sub-solution.

To prove that u_* is a super-solution, let $\varphi \in C^\infty(\mathbb{R}^2 \times \mathbb{R}^+)$ and (x_0, t_0) a minimum point of $u_* - \varphi$ in $\mathbb{R}^2 \times \mathbb{R}^+_*$.

Again we obviously get

$$\frac{\partial u}{\partial t}(x_0, t_0) = \frac{\partial \varphi}{\partial t}(x_0, t_0) = 0.$$

Then the super-solution condition is

$$\frac{\partial \varphi}{\partial t}(x_0, t_0) = 0 \geq -(-(curv(\varphi(x_0, t_0))_-)^p |D\varphi(x_0, t_0)|$$

and it is empty. ◇

Corollary 1 *Let S_0 be a connect and bounded shape, and the multiscale analysis given by the equation (29). Then the asymptotic state of S_0 under the action of the above multiscale analysis is given by the convex-hull of S_0, i.e., S_0^c. That is*

$$\lim_{t \to +\infty} T_t(S_0) = S_0^c.$$

Proof : Using the preceding proposition, we have that

$$T_t(S_0^c) = S_0^c \quad \forall t > 0.$$

Since $(T_t(S_0))_{t>0}$ is increasing family sets included in S_0^c, there exists S_∞ such that

$$\lim_{t \to \infty} T_t(S_0) = \bigcup_{t>0} T_t(S_0) = S_\infty.$$

Wherever the set S_∞ has a finite curvature, it is positive since $T_t(S_\infty) = S_\infty$ for any $t > 0$. Where the set S_∞ has a corner, it has to be a "convex" one by a remark did in the proof of the preceding proposition. Hence the set S_∞ is convex. But, since $S_0 \subset S_\infty$, by definition of S_0^c, we conclude that $S_0^c = S_\infty$. ◇

Corollary 2 *If all the connect components of a shape S_0 are convex and S'_0 is another shape which have one connect component which is non-convex, then for some $t \geq 0$ and for the multiscale analysis associated to the equation (29),*

$$|S'(t)| \neq |S(t)|.$$

Proof : Using the preceding proposition, we have that $T_t(S_0)$ is constant for all scale $t \geq 0$. But $T_t(S'_0)$ will change because of the non-convex connect component; precisely it will increase. ◇

Proposition 7 *Let S and S' be two regular shapes. If the evolutions of their areas are the same for all the multiscale analyses, i.e., $|S'_{(p,\beta_{-1},\beta_1)}| = |S_{(p,\beta_{-1},\beta_1)}|$ and for all scales, then they have the same perimeter.*

Proof : The assumption gives

$$-\int_0^{2\pi} k^p v du = -\int_0^{2\pi} k'^p v' du \quad \text{for all } p > 0.$$

We wish to let p go to 0 but it is an easy application of the Lebesgue's Lemma since kv is bounded by regularity of shapes. ◇

References

[1] Alvarez L., Blanc A-P., Mazorra L. and Santana F. *Geometric Flows and Global Invariant Signatures* Cuadernos del Instituto Universitario de Ciencias y Tecnologas Cibernticas Vol 15, pp. 1-23.

[2] Alvarez L., Mazorra L. and Santana F. *Geometric Invariant Shape Representation using Morphological Multiscale Analysis* Cuadernos del Instituto Universitario de Ciencias y Tecnologas Cibernticas Vol 16, pp. 1-20

[3] Alvarez L., Guichard F., Lions P.-L. and Morel J-M., *Axioms and fundamental equations in image processing*, Arch. Rational Mech. Anal., Vol. 123, 199–257, 1993.

[4] Alvarez L. and Morel J-M., *Formalization and Computational Aspects of Image Analysis,* Acta Numerica pp. 7-59, 1994.

[5] Angenent S., *Parabolic equations for curves on surfaces, Part I. Curves with p-integrable curvature*, Annals of Mathematics Vol. 132, 451-483, 1990.

[6] Angenent S., *Parabolic equations for curves on surfaces, Part II. Interseccions blow-up, and generalized solutions*, Annals of Mathematics Vol. 133, 171-215, 1991.

[7] Angenent S., Sapiro G. and Tannenbaum A., *On the affine heat equation for nonconvex curves*, Journal of the American Mathematical Society Vol. 11, no. 3, 601–634, 1998.

[8] Asada H. and Brady M.. The curvature primal sketch, IEEE Transactions on PAMI, Vol. 8, 2-14, 1986

[9] Cao F. and Moisan L., *Geometric computation of curvature driven plane curve evolutions*, SIAM Journal of Numerical Analysis, Vol. 39-2, 624–646, 2001

[10] Crandall M.G., Ishii H., Lions P.-L., User's guide to viscosity solutions of second order partial differential equations, *Bull. AMS* 27, 1-67, 1992

[11] Cohignac T. and Lopez C. and Morel J-M., *Integral and local affine invariant parameter and application to shape recognition*, Proceedings of ICPR conference, A:164–168, 1994.

[12] Cohignac T. and Morel J-M., *Scale space and affine invariant recognition of occluded shapes*, Proceedings of Spie conference, investigate and trial image processing, Vol. 2567, 214–222, 1995.

[13] Lisani J.L., Moisan L., Monasse P., and Morel J-M., *Affine invariant mathematical morphology applied to a generic shape recognition algorithm.* In Mathematical Morphology & its Applications to Image & Signal Process. Vol. 18. Kluwer Academic Publishers.

[14] Gage M., *An isoperimetric inequality with applications to curve shortening*, Duke Mathematical Journal , Vol. 50, No. 4, 1225-1229, 1983.

[15] Gage M., *Curve shortening makes convex curves circular*, Inventiones Mathematicae, Vol. 76, 357-364, 1984.

[16] Gage M. and Hamilton R.S., *The heat equation shrinking convex plane curves*, J. Differential Geometry, Vol. 23, 69–96, 1986.

[17] Grayson M. , *The heat equation shrinks embedded plane curves to round points*, J. Differential Geometry, Vol 26, 285–314, 1987.

[18] Guichard F. and Morel J-M. *Image Analysis and P.D.E.'s* to appear.

[19] Ishii H. & Souganidis P. *Generalized motion of noncompact hypersurfaces with velocity having arbitrary growth on the curvature tensor* Tohoku mathematical journal, 47(2), June 1995, 227-250

[20] Kimia B. and Tannenbaum A. and Zucker S. *Shapes, shocks, and deformations I: the components of two-dimensional shape and the reaction-diffusion space* International Journal of Computer Vision, vol. 15, pp189-224, 1995.

[21] Loncaric S. *A Survey of Shape Analysis Techniques*. Pattern Recognition, Vol. 31, No. 8, pp. 983-1001, 1998

[22] Maragos P. *Pattern spectrum and multiscale shape representation.* IEEE Transactions on Pattern Analysis and Machine intelligence, 11(7):701-716, July 1989.

[23] Mokhtarian, F. Abbasi S. and Kittler J. *Robust and Efficient Shape Indexing through Curvature Scale Space* in Proceedings of the sixth British Machine Vision Conference, BMVC'96. Edinburgh, 10-12 September 1996, pp 53-62.

[24] Mokhtarian, F. Abbasi S. and Kittler J. *Efficient and Robust Retrieval by Shape Content through Curvature Scale Space* in Proceedings of the First International Workshop on Image Database and Multimedia Search, Amsterdam, The Netherlands Aug 1996, pp 35-42.

[25] Mokhtarian, F. and A. K. Mackworth, *A Theory of Multi-Scale, Curvature-Based Shape Representation for Planar Curves*, IEEE Trans. Pattern Analysis and Machine Intelligence, vol. 14, no. 8, pp. 789-805, 1992.

[26] Pavlidis T., *A review of algorithms for shape analysis*, Computer Graphics Image Processing, vol. 7, pp. 242–258, 1978.

[27] Sapiro G. and Tannenbaum A., *Affine invariant scale space*, International Journal of Computer Vision, Vol 11, 25–44, 1993.

[28] Sethian J., *Level set methods*, Cambridge University Press, 1996.

[29] Souganidis P. *Front propagation: Theory and Applications*, CIME Course on Viscosity Solutions, Lect. Notes in Math. 1660, Springer-Verlag, 1997.

[30] Witkin A. *Scale space filtering:A new approach to multi-scale description.* In S. Ullman and W. Richards, editors, Image Understanding 1984, Ablex, New Jersey, 1984.

Instituto Universitario de Ciencias y Tecnologías Cibernéticas
Universidad de Las Palmas de Gran Canaria
Campus de Tafira
35017 Las Palmas, España
http://www.iuctc.ulpgc.es